



3

4 Dongmin Kim^{1,2}, Andrew C. Ross³, Sang-Ik Shin^{4,5}, Fabian A. Gomez^{6,2}, Jasmin G. John²,
5 Denis L. Volkov^{1,2}, Sang-Ki Lee², Michael A. Alexander⁷ and Charles A. Stock³

6

⁷ Cooperative Institute for Marine and Atmospheric Studies, University of Miami, Miami, FL,
⁸ USA

⁹NOAA/OAR/Atlantic Oceanographic & Meteorological Laboratory, Miami, FL, USA

³ NOAA/OAR/Geophysical Fluid Dynamics Laboratory, Princeton, NJ, USA,

⁴Cooperative Institute for Research in Environmental Sciences, University of Colorado Boulder

12 Boulder, CO, USA,

¹³ NOAA/OAR/Physical Sciences Laboratory, Boulder, CO, USA

6Northern Gulf Institute, Mississippi State University

45 $^7\text{D}_2$ state of Au^{+} in 1O_2 solution. University of Guelph, P.

20

21 Marine and Atmospheric Studies, University of Miami, 4600 Rickenbacker Causeway, Miami, FL
22 33149, USA.

23



24 **Abstract**

25 We used a high-resolution (1/12°) Modular Ocean Model version 6 implementation for the
26 the Northwest Atlantic Ocean (MOM6-NWA12) to dynamically downscale Geophysical Fluid
27 Dynamics Laboratory Earth System Model version 4.1 (GFDL-ESM4.1) projections for the 21st
28 century. Simulations were conducted under four different Coupled Model Intercomparison
29 Project Phase 6 emission scenarios. MOM6-NWA12 accurately simulates the spatial patterns of
30 sea surface temperature, salinity, and dynamic sea surface height (SSH) during the historical
31 period. In particular, the Gulf Stream's strength, position, recirculation, and separation from the
32 U.S. East Coast are significantly improved in MOM6-NWA12 compared to the coarse-resolution
33 GFDL-ESM4.1. Projected end-of-century warming varied strongly between scenarios, from ~
34 4 °C under prior "worst case" emissions scenarios (SSP-585), 2~3 °C under intermediate
35 scenarios (SSP-245, SSP-370) more consistent with current trajectories, to ~ 1oC under
36 aggressive mitigation (SSP-126). Consistent with a significant weakening of the Atlantic
37 Meridional Overturning Circulation projected by GFDL-ESM4.1, MOM6-NWA12 shows a
38 substantial volume transport reduction in the Western Boundary Current (WBC) system (i.e.,
39 Yucatan Current, Florida Current, Antilles Current, and the Deep Western Boundary Current)
40 toward the late 21st century (between 23 and 38 %, varying by scenario). This projected
41 weakening of the WBC system and the associated reduction in the coastal upwelling of cold,
42 fresh subsurface waters lead to a significant increase in ocean temperature, salinity, and dynamic
43 SSH along the U.S. southeast and northeast Coasts, particularly in the South Atlantic Bight.
44 These localized changes have significant implications for future sea level rise, marine
45 ecosystems, and fish populations in these highly vulnerable regions.

46



47 **1. Introduction**

48 The Northwest Atlantic Ocean (NWA), including the United States (US) East and Gulf
49 Coasts, and the Caribbean Sea, is characterized by large spatial heterogeneity in ocean conditions
50 and complex interactions between ocean circulation and biogeochemistry (e.g., Wang et al.,
51 2013; Muller-Karger et al, 2015; Wanninkhof et al., 2015; Gomez et al., 2020; 2022; Friedrichs
52 et al., 2019; Zhang et al., 2023). A myriad of living marine resources inhabit this region,
53 including the South Florida coral reefs, lobsters and shellfish, demersal fish species like
54 groupers, snappers, cod and haddock, and migratory pelagic fish species like bluefin tuna and
55 king mackerel, all of whose distribution and abundance are influenced by changes in ocean
56 temperature and circulation (e.g., Weinberg 2005; Bell et al., 2015; Karnauskas et al., 2013,
57 2015; Tanaka et al., 2020). Previous studies have shown that portions of the ocean ecosystem are
58 modulated by large scale climate variability, such as El Niño Southern Oscillation and Atlantic
59 Multidecadal Oscillation, through associated changes in ocean circulation and river runoff (e.g.,
60 Alexander and Scott, 2008; Gomez et al., 2019, 2024). Moreover, the region is undergoing
61 sustained warming, particularly along the US South and East Coasts, where the surface
62 temperature warming rate was about two or three times faster than that of the global ocean
63 average for 1970-2020 (e.g., Pershing et al., 2015; Wang et al., 2023).

64 Previous studies have also attributed regional acceleration and spatial variation of the US
65 East Coast sea level rise to ocean circulation changes, including a weakening of the Gulf Stream
66 (e.g., Ezer et al., 2013; Ezer, 2015; Goddard et al., 2015; Park and Sweet, 2015; Dong et al.,
67 2019), warming of the Gulf Stream and the entire subtropical gyre (e.g., Domingues et al., 2018;
68 Volkov et al., 2019, 2023; Steinberg et al., 2024; Huang et al., 2025), and a slowdown of the
69 Atlantic Meridional Overturning Circulation (AMOC, e.g., Levermann et al., 2005; Little et al.,



70 2017, 2019). While progress has been made in understanding ocean conditions off the US East
71 and Gulf Coasts and in the Caribbean Sea, substantial uncertainties still remain regarding future
72 changes in regional ocean circulation and their sensitivity to greenhouse gas emissions scenarios.
73 Consequently, it is essential to investigate projected changes in ocean circulation across
74 scenarios to improve our understanding of future ocean conditions and ecosystem dynamics
75 across the Northwest Atlantic.

76 Global models, such as General Circulation models (GCMs) and Earth System Models
77 (ESMs), offer valuable insights into future ocean conditions under various climate scenarios.
78 However, they are often limited in spatial resolution due to computational constraints and may
79 face significant uncertainties due to limitations in representing the fine-scale ocean circulation
80 and thermohaline structures, particularly in coastal regions. Hence, high-resolution, eddy-
81 resolving ocean models are critical for addressing these limitations, providing improved
82 representations of historical ocean circulation across multiple timescales and offering more
83 reliable future projections (e.g., Drenkard et al., 2021). To leverage the benefits of resolving
84 eddies and shelf-scale circulation while lowering the computational burden, multiple studies
85 have applied dynamic downscaling techniques to better understand and project regional impacts
86 of climate change on NWA ocean systems (e.g., Liu et al., 2012, 2015; Alexander et al., 2020;
87 Shin and Alexander, 2020; Rutherford et al., 2024).

88 By refining the outputs of GCMs/ESMs using high-resolution regional models, dynamical
89 downscaling can capture finer-scale processes and interactions that are often missed by coarse-
90 resolution models. For example, the projected weakening of the Loop Current and associated
91 reduction in warm water transport through the Yucatan Channel are poorly resolved in Coupled
92 Model Intercomparison Project Phase 5 (CMIP5) and CMIP6 global models, leading to an



93 overestimation of SST warming over the northern part of the Gulf of America (GoA; a.k.a. Gulf
94 of Mexico) and underestimation of SST warming along the West Florida shelf - an issue better
95 addressed by high-resolution downscaled models (e.g., Liu et al., 2012, 2015). Similarly,
96 systematic CMIP model biases in the Gulf Stream representation led to under-estimation of
97 warming of Northeast U.S. waters associated with future changes in the Gulf Stream path (Saba
98 et al., 2016).

99 In line with these efforts, the National Oceanic and Atmospheric Administration (NOAA)
100 Changing Ecosystems and Fisheries Initiative (CEFI) modeling team has developed a high-
101 resolution regional ocean model - the Modular Ocean Model version 6 at 1/12° horizontal
102 resolution (~ 8 km) for the Northwest Atlantic Ocean (MOM6-NWA12; Ross et al., 2023).
103 MOM6-NWA12 is configured to capture key regional features and simulate ocean dynamics in
104 the Northwest Atlantic with high fidelity. This model provides a valuable framework for
105 studying the complex interactions between large-scale processes and local features that govern
106 both physical and biogeochemical variability in the region. MOM6-NWA12 demonstrates strong
107 performance in reproducing a broad range of observed physical and biogeochemical conditions
108 during the hindcast period (1993-2020, Ross et al., 2023). Furthermore, it exhibits skillful
109 seasonal to decadal forecast capabilities for SST anomalies (SSTAs, Koul et al., 2024; Ross et
110 al., 2024). However, while MOM6-NWA12 has shown promise for seasonal and decadal
111 predictions, its potential for multi-decadal (30~100 years) projections remains unexplored.

112 In this study, we use the high-resolution MOM6-NWA12 model to dynamically downscale
113 future projections from the Geophysical Fluid Dynamics Laboratory's Earth System Model
114 version 4.1 (GFDL-ESM4.1) for the Northwest Atlantic Ocean. With this downscaling
115 procedure, we aim to generate more accurate and regionally relevant projections of future ocean



116 conditions. Unlike prior studies, which used a single greenhouse gas emissions scenario, we
117 consider the range of potential ocean futures from projections using four different scenarios (i.e.,
118 Shared Socioeconomic Pathways; SSP-126, SSP-245, SSP-375, and SSP-585) spanning
119 aggressive mitigation to high emissions pathways beyond our current trajectory. This allows us
120 to identify the NWA responses to future climate change that are sensitive to emissions pathways
121 from those that are not, and to explore mechanisms underlying these contrasts. We also build on
122 prior work to understand regional hot-spots of ocean change and their drivers. This approach
123 enhances our understanding of regional ocean dynamics and supports the development of
124 effective mitigation and adaptation strategies in response to climate change.

125

126 **2. Model and downscaling settings**

127 2.1 MOM6-NWA12

128 MOM6-COBALT-NWA12 is a coupled ocean circulation and sea ice model which can also
129 include coupled ocean biogeochemistry (Ross et al., 2023). Here, we consider a “physics-only”
130 implementation of this system (i.e., MOM6-NWA12), which has also been applied for seasonal
131 and decadal prediction applications (Ross et al., 2024; Koul et al., 2024). The model spans the
132 Northwest Atlantic Ocean, including the Caribbean Sea, the Gulf Coast, and the U.S. East Coast
133 98°W-36°W and 5°N-52°N, and has 775×845 grid points (Fig. 1). The nominal horizontal
134 resolution is about 1/12°. The zonal distance between grid points varies with latitude, from ~9
135 km at the southern boundary to ~5 km at the northern boundary. The model has 75 vertical
136 layers using a z^* -coordinate, a depth coordinate rescaled with the free surface (Adcroft and
137 Campin, 2004). The vertical resolution is finest near the surface, where the layer thickness is 2
138 m, increasing gradually with depth to a maximum thickness of 250 m above the deepest model



139 depth of 6500 m. The model's subgrid-scale parameterizations are adapted from the 1/4° global
140 MOM6, with updates and modifications to account for the increased horizontal resolution (Ross
141 et al., 2023). MOM6-NWA12 has the option of using time steps for thermodynamics and ocean-
142 biogeochemistry longer than the baroclinic time step, which significantly reduces the running
143 time for coupled model simulations. More detailed model description, additional features, and
144 parameterization settings can be found in Ross et al. (2023).

145

146 2.2 GFDL-ESM4.1

147 NOAA GFDL's Earth System Model version 4.1 (GFDL-ESM4.1, Dunne et al. 2020)
148 provides the boundary conditions for the MOM6-NWA12 simulations. We carried out four sets
149 of MOM6-NWA12 simulations downscaling GFDL-ESM4.1 simulations under SSP-126, SSP-
150 245, SSP-375, and SSP-585 scenarios (O'Neill et al., 2016). GFDL-ESM4.1 is built on a basis of
151 GFDL's AM4.0 atmospheric model, which has 49 hybrid vertical layers and approximately 1° ×
152 1° horizontal resolution (Zhao et al., 2018a, 2018b), using the Finite Volume version 3 (FV3;
153 Lin, 2004) dynamical core with advanced parameterizations of moist convection, clouds,
154 radiation, topographical drag, and several other physical processes from its previous version. The
155 land model in GFDL-ESM4.1 is GFDL's Land Model version 4.1 (LM4.1; Shevliakova et al.,
156 2024), which improved radiative properties for vegetation, soil, and snow, and updated
157 hydrology in LM4.0. The ocean model component of GFDL-ESM4.1 uses MOM6 (Adcroft et
158 al., 2019), configured with 75 vertical hybrid coordinate layers within the Arbitrary-Lagrangian-
159 Eulerian algorithm (Adcroft & Hallberg, 2006), and the GFDL's Sea Ice Simulator (SIS2;
160 Adcroft et al., 2019). More detailed model description, additional features, and parameterization
161 settings of GFDL-ESM4.1 can be found in Dunne et al. (2020).



162

163 2.3 Reanalysis datasets

164 The global reanalysis datasets used to force the retrospective ocean simulation of Ross et al.
165 (2023) are also used here for bias corrections of ocean lateral boundary conditions, surface
166 forcings, and river discharge for the historical and future projections derived from GFDL-
167 ESM4.1 (Table 1). We use the high-resolution (1/12°) Global Ocean Physics Reanalysis
168 (GLORYS12; Lellouche et al., 2021) to derive monthly ocean temperature, zonal and meridional
169 speeds of ocean current, salinity, and sea surface height (SSH) for 1993-2020 period. We also
170 use 3-hourly European Centre for Medium-Range Weather Forecast (ECMWF) Reanalysis
171 version 5 (ERA5) atmospheric reanalysis datasets to derive near-surface zonal and meridional
172 winds, near-surface air temperature, specific humidity, precipitation, and downwelling short- and
173 long-wave radiative fluxes (Hersbach et al., 2020). For river discharge, we use the gridded daily
174 Global Flood Awareness System (GloFAS) version 3.1 reanalysis (Alfieri et al., 2020).

175

176 **Table 1.** Reanalysis products and associated variables used for the bias correction and validation
177 in this study.

Reanalysis product	Variables	Frequency
ERA5	2 m temperature	3 hourly
	2 m specific humidity	3 hourly
	10 m zonal wind	3 hourly



	10 m meridional wind	3 hourly
	Sea level pressure	Daily
	Liquid precipitation rate	Daily
	Snowfall rate	Daily
	Downward shortwave radiative flux	Daily
	Downward longwave radiative flux	Daily
GLORYS12	Sea water potential temperature	Monthly
	Sea water salinity	Monthly
	Sea water zonal velocity	Monthly
	Sea water meridional velocity	Monthly
	Sea surface height	Monthly
GloFAS	River runoff rate	Daily

178

179 2.5 Mean bias correction

180 To reduce systematic biases in the GFDL-ESM4 outputs, we applied a climatological mean
181 bias correction to the lateral ocean boundary conditions (BCs) and surface atmospheric forcing
182 fields using the GLORYS12 and ERA5 reanalysis datasets as follows:

183 Bias-corrected variables = GFDL-ESM4 + Delta

184 Delta = <Reanalysis> - <GFDL-ESM4>



185 where the GFDL-ESM4 refers to the raw outputs from the GFDL-ESM4 simulations.
186 <Reanalysis> and <GFDL-ESM4> are the long-term averaged annual cycles from the reanalysis
187 and GFDL-ESM4 simulations for the 1993-2020 period, respectively. For the GFDL-ESM4
188 simulations, we merged the data from its historical simulation (1993-2014) with the data from
189 the future period in each of the four SSP scenarios (2015-2020). The long-term (1993-2020)
190 means for each month of the year determine the mean annual cycle of the ocean variables, while
191 the long-term means for each 3-hourly frequency of the year determine the mean annual cycle of
192 the atmospheric variables. The mean bias correction terms, Delta, were then added to the GFDL-
193 ESM4 outputs for the entire simulation period (1950-2100) to correct the mean biases. This bias
194 correction method ensures that mean states of MOM6-NWA12 during the historical period
195 (1993-2020) are comparable to those in the reanalysis datasets and in Ross et al., (2023).

196 Our “Delta method” fundamentally differs from the previous ones used for dynamical
197 downscaling. While previous studies (Liu et al., 2012; 2015; Alexander et al., 2020; Shin and
198 Alexander, 2020; Pozo-Buil et al., 2021) assumed that climate variability remains the same as
199 the historical period for future projections, we retained the model-generated climate variability
200 for more consistent climate projections, since weather and climate are interdependent. Indeed,
201 not only does weather depend strongly on low-frequency variability (e.g., weather conditions
202 during the different phases of ENSO are substantially different), but also weather statistics can
203 substantially change under future climate conditions (e.g., Cheng et al., 2012; Jeong and
204 Sushama, 2019). In addition, since the uncertainty of both future precipitation change and its
205 impact on runoff are high (e.g., Giuntoli et al., 2015; Jackson and Wood, 2018), we did not
206 consider the future changes in runoff here in this single-model downscaling. Therefore, we



207 applied the daily mean climatology (1993-2020) of GloFAS river runoff data for the entire
208 simulation period (1950-2100).

209 A second notable difference between the methodology herein and past Northwest Atlantic
210 downscaling studies is the replacement of limited “time slice” experiments with a continuous
211 integration over the historical and future periods. The continuous integration approach requires
212 more computational investment (time slices were generally compared across 10-30 year intervals
213 while continuous integrations required 150 years), but it allows for a more complete analysis of
214 the emergence of significant differences between scenarios and historical conditions, and
215 between the scenarios themselves (e.g., Drenkard et al., 2021).

216 Finally, for sea level, we note that both GFDL-ESM4.1 and MOM6-NWA12 utilize the
217 Boussinesq approximation. This implies that the global mean sea level rise (or variability) is
218 missing in both models (e.g., Greatbatch, 1994; Griffies and Greatbatch, 2012; Griffies et al.,
219 2014). Since SSH in GFDL-ESM4.1 (“zos” in the model’s output files) is the ocean dynamic sea
220 level anomaly, the bias-corrected SSH was averaged over the model domain for the entire period
221 (1850-2100) and subtracted from the bias-corrected SSH at each grid point along the model
222 boundaries to make sure that the basin-averaged SSH anomalies in MOM6-NWA12 do not vary
223 in time.

224

225 **3. Results**

226 3.1. Model validation for the historical period

227 To evaluate the performance of GFDL-ESM4.1 and MOM6-NWA12 in the historical period,
228 we first compared model-derived climatologies of SST, sea surface salinity (SSS), and surface
229 current speed against the GLORYS12-derived climatological patterns (Fig. 2 and 3). The GFDL-



230 ESM4.1 outputs show considerable biases in the SST and SSS mean patterns. Specifically, the
231 SST has a warm bias $>3^{\circ}\text{C}$ in the Mid-Atlantic Bight (MAB), and a cold bias $>2^{\circ}\text{C}$ in magnitude
232 along the North Atlantic Current path compared to the data-assimilative GLORYS12 product
233 (Fig. 3a). GFDL-ESM4.1 SSS is saltier than the GLORYS SSS over the entire domain (Fig. 3b),
234 especially in the MAB and along the US Gulf Coast, where the bias reaches values >3 PSU.
235 These biases are greatly reduced in the MOM6-NWA12. For example, the SST biases in the
236 MAB and along the Gulf Stream are $\sim 1^{\circ}\text{C}$ or lower (Fig. 3d). The SSS shows a small negative
237 bias, except over the Gulf of Maine, where SSS is overestimated by about 0.7 PSU (Fig. 3e).

238 The bias patterns for surface ocean velocity reveal that ESM4.1's Loop Current is more
239 diffusive and extended more northward compared to that in GLORYS12 (Fig. 3c). This appears
240 to be due to the coarse horizontal resolution of GFDL-ESM4.1 ($\sim 0.5^{\circ}$), which is not fine enough
241 to resolve the Loop Current dynamics (e.g., Liu et al., 2012; 2015). In addition, ESM4.1's Gulf
242 Stream along the South Atlantic Bight (SAB) is weaker and shifted away from the US East Coast
243 compared to that in GLORYS12. In contrast, MOM6-NWA12 shows much improvement of both
244 the Loop Current and Gulf Stream System (Fig. 2i and Fig. 3f). For instance, the Florida Current
245 (beginning of the Gulf Stream System) in MOM6-NWA12 flows closer to the coastline
246 compared to that in GFDL-ESM4.1 with speeds exceeding 1 m s^{-1} , a pattern similar to
247 GLORYS12 (Fig. 2i and Fig. 3f).

248 After the separation of the Gulf Stream from the US East Coast, the sluggish flow in GFDL-
249 ESM4.1 is shifted northward compared to GLORYS12, both at its separation point and as it
250 travels eastward across the North Atlantic (Fig. 2f and Fig. 3c). In contrast, the faster Gulf
251 Stream in MOM6-NWA12 (Fig. 2i and Fig. 3f) is shifted southward at its separation from the
252 coast before regaining consistency with the data-assimilative GLORYS12 path to the east. This



253 is more clearly shown in Supplementary Fig. S1, which shows the position of the Gulf Stream
254 core as a 15°C isotherm at 200m (e.g., Sanchez-Franks and Zhang, 2015; Hameed et al., 2018;
255 Seidov et al., 2019; Ross et al., 2023). A northward shift in the Gulf Stream position is typical in
256 low-resolution ocean models and has been attributed to misrepresentation of nonlinear vorticity
257 boundary dynamics. While it is not clear why the Gulf Stream in MOM6-NWA12 is shifted
258 southward, previous studies have indicated that the separation of the Gulf Stream in an eddy-
259 resolving model is very sensitive to the choices made for subgrid scale parameterizations (e.g.,
260 Chassignet and Marshall, 2008).

261 Consistent with the surface current speed and position of the Gulf Stream, GFDL-ESM4.1
262 displays a large negative bias in the dynamic sea surface height (SSH), immediately south of the
263 Gulf Stream core and its extension to the North Atlantic Current. Connected with this, the
264 recirculation gyre south of the Gulf Stream (35°N- 73°W), known as the Worthington Gyre
265 (Worthington, 1976), is almost completely absent in GFDL-ESM4.1 (Fig. 4b and d). On the
266 other hand, the spatial pattern of the dynamic SSH in MOM6-NWA12 exhibits improved
267 agreement with that in GLORYS12 (Fig. 4c and e), reproducing a Worthington Gyre albeit
268 weaker than GLORYS12. Given that the Worthington Gyre is a long-term mean rectification of
269 the Gulf Stream rings and instability waves not resolved at coarse resolution, it is not surprising
270 that the recirculation gyre is better represented in MOM6-NWA12 while it is nearly absent in
271 GFDL-ESM4.1.

272 Lastly, we evaluated the volume transports of Northwestern Atlantic boundary current
273 systems across four zonal transects for the Yucatan Current, Florida Current, Antilles Current,
274 and the Deep Western Boundary Current (DWBC) as shown in Fig. 5. The zonal transection
275 lines for the four current systems are shown in Fig. 1 (red solid lines). The Antilles Current



276 transport was obtained by integrating the meridional flow over the upper 500 m across 26.5°N
277 and 77.5°W-75°W. Similarly, the DWBC transport was obtained by integrating the meridional
278 velocity between 1,000m and 5,000m across 26.5°N and 77.5°W-75°W. GFDL-ESM4.1
279 simulates a Yucatan Current transport of 43.9 ± 2.87 Sv, which is about 62% larger than in-situ
280 observation of 27.5 ± 2.6 Sv (Athié et al., 2020, Fig. 5a). In contrast, MOM6-NWA12 simulates
281 a transport of 24.2 ± 1.7 Sv, which agrees much better with the observed transport. However, the
282 Florida Current (80°W-77.5°W) transport simulated by MOM6-NWA12 (24.3 ± 1.6 Sv)
283 underestimates the observation (32.5 ± 3.2 Sv in Volkov et al., 2024), whereas the Florida
284 Current transport simulated by GFDL-ESM4 (34.4 ± 2.5 Sv) is comparable to the observation.
285 This occurs despite far more realistic surface current speeds in MOM6-NWA12 (i.e., Fig. 2)
286 because the ESM4.1 Florida Current is far more diffuse and extends to greater depth. Additional
287 sensitivity simulations indicate that the Florida Current transport in MOM6-NWA12 is quite
288 sensitive to the eddy viscosity (not shown). By increasing the model diffusivities in MOM6-
289 NWA12, the simulated Florida Current transport also increased closer to the observed value.
290 However, this occurred at the expense of other model features, such as the latitude of Gulf
291 Stream separation from the coast, becoming less realistic. Therefore, the momentum and density
292 diffusivities for MOM6-NWA12 are unchanged from those used in Ross et al. (2023).
293 As shown in Fig. 5c and d, the simulated transports for both the Antilles Current (12.3 ± 4.1
294 Sv) and the DWBC (-20.8 ± 8.8 Sv) in the GFDL-ESM4.1 show substantial disagreement with
295 observations (4.7 ± 5.2 Sv for the Antilles Current, Meinen et al., 2019; and -31.2 ± 5.5 Sv for
296 the DWBC, Zantopp et al., 2017). MOM6-NWA12, in contrast, better reproduced both the
297 Antilles Current (3.4 ± 5.6 Sv) and the DWBC (-35.2 ± 9.5 Sv). The large biases in GFDL-



298 ESM4.1 appear to be linked to the overly diffusive and broad Antilles Current and DWBC
299 (Supplementary Fig. S2).
300 Overall, the high-resolution MOM6-NWA12 configuration generally shows large
301 improvement in simulating regional ocean circulation and mean conditions compared to the low-
302 resolution GFDL-ESM4.1. Some deficiencies, however, still exist. Potential impacts of these
303 deficiencies on projected changes, and pathways for future model improvement, will be
304 discussed in Section 4.
305
306 3.2. Future projections
307 3.2.1. SST and SSS
308 We first examine the projected spatial changes in SST and SSS derived from the MOM6-
309 NWA12, comparing the historical period (HIST: 1993–2020) with the late 21st century (L21C:
310 2073–2100) across four SSP scenarios (SSP-126, SSP-245, SSP-370, and SSP-585). MOM6-
311 NWA12 shows that SST changes in the future exhibit basin-wide warming with discernable end-
312 of-century differences (Fig. 6a–e). The domain-averaged SST warming is lowest in the SSP-126
313 (0.52 °C) simulation and intensifies progressively in SSP-245 (1.21 °C), SSP-370 (1.86 °C) and
314 SSP-585 (2.23 °C) simulations. The SST increase is particularly large in the MAB, the Gulf of
315 Maine, and around the Georges Bank. Temperatures are projected to warm by 4°C in some areas
316 in the SSP-585 scenario (Fig. 6e). Warming in these regions is reduced to ~3°C, ~2°C and ~1°C
317 in SSP-370, SSP-245 and SSP-126, respectively (Fig. 6b–d). Mean warming over the next 30
318 years (2025–2055), is expected to ~1–2°C with less separation between scenarios (Supplementary
319 Fig. S3).



320 Similar to the SST change, the amplitude of the SSS change is sensitive to the SSP scenarios
321 (Fig. 6f-j). The increase in domain-averaged SSS is more pronounced in the higher emission
322 scenarios (0.13 PSU for SSP-126, 0.22 PSU for SSP-245, 0.41 PSU for SSP-370, and 0.46 PSU
323 for SSP-585). While SSS tends to increase in the subtropical part of the domain, the largest
324 projected SSS increase is along the SAB, the continental slope off the MAB and the West
325 Florida Shelf where the future change intensifies progressively under the high-emission scenario.

326 The large increases in SST and SSS on the West Florida Shelf and the SAB appear to be
327 linked to a reduction in shelf-break upwelling due to the projected weakening of the Loop
328 Current and Gulf Stream (Fig. 7). Additionally, the weakening of the Gulf Stream leads to a
329 northward shift after its separation from the US East Coast in the late 21st century in all four SSP
330 scenarios (Fig. 7, Section 3.2.2), consistent with previous studies (e.g., Saba et al., 2016; Caesar
331 et al., 2018; Bellomo et al., 2021). It appears that the SST increase along the edge of the MAB is
332 linked to the northward shift of the Gulf Stream and the implied warm water intrusion to the
333 Slope Sea (Saba et al., 2016). Warming via this mechanism is fortified by commensurate mean
334 reductions of the advection of cold high-latitude waters from the Labrador Sea. Interestingly, a
335 narrow region of minimal surface warming is evident immediately south of the historical Gulf
336 Stream path (Fig. 6e). A similar, but smaller area of minimum surface warming is also evident in
337 the northern GoA, which is largely consistent with previous studies (Liu et al., 2012, 2015).
338 These regions of minimal SST warming appear to be linked to the northward shift of Gulf
339 Stream or the reduced Loop Current, implying a reduction in ocean heat transport to these
340 regions (Figs. 6e and 7j).

341 While GFDL-ESM4.1 shows the SSP scenario sensitivity for the amplitude of the future SST
342 and SSS changes, the pronounced SST warming identified by MOM6-NWA12 in the Mid-



343 Atlantic Bight (MAB) and Gulf of Maine regions is almost completely absent in GFDL-ESM4.1
344 (Supplementary Fig. S4). This is consistent with the absence of a future northward shift in the
345 Gulf Stream in the coarse resolution GFDL-ESM4.1 (Supplementary Fig. S5) and prior findings
346 of Saba et al., 2015.

347 In summary, MOM6-NWA12 projections of SST, SSS, and surface current speed indicate
348 that under all four future scenarios, the Northwestern Atlantic basin becomes significantly
349 warmer, and saltier especially along the US East Coast and the West Florida shelf regions, and
350 the Gulf Stream becomes considerably weaker and shifts northward. The magnitude of projected
351 end-of-century changes, however, varies considerably across scenarios. Most notably, the
352 severity of the impacts projected by the prior worst-case scenario in CMIP5 (i.e., RCP 8.5) are
353 progressively mitigated by lower emissions scenarios. Differences between scenarios, however,
354 are far smaller in the first half of the century.

355

356 3.2.2. WBC transports

357 As shown in Figs. 7, the entire WBC system, including the North Brazil Current, Caribbean
358 Current, Yucatan Current, Loop Current, Florida Current, and the Gulf Stream, weakens, at least
359 at the surface, consistent with previous future projection studies (e.g., Liu et al., 2012, 2015;
360 Saba et al., 2016; Alexander et al., 2020; Shin and Alexander, 2020). The consistency of the
361 surface speed changes across scenarios suggests that the policy differences between scenarios
362 may have limited impact on Gulf Stream properties in the NWA. Inspection of volume
363 transports, however, shows that differences do emerge by the end of the century (Fig. 8).

364 The Florida Current exhibits a gradual decline throughout the 21st century across all SSP
365 scenarios. The largest decrease in the late 21st century is shown in the SSP-585 scenario (Fig.



366 8a), from 24.2 ± 1.7 Sv in the historical period to 15.2 ± 3.5 Sv in the late 21st century (37.2 %
367 decline) while the smallest decrease in the late 21st century is shown in the SSP-126 scenario
368 (24.3% decline). The intermediate cases more consistent with current CO₂ trajectories also
369 exhibit smaller shifts than the prior worst case. The Yucatan Current shows similar rates of
370 decrease and scenario sensitivity. Under SSP-585, the Yucatan Current transport decreased from
371 21.0 ± 2.1 Sv in the historical period to 13.2 ± 3.1 Sv in the late 21st century (37.1 % decline,
372 Fig. 8b) but end-of-century declines are partially mitigated at intermediate and low emissions
373 cases. The mean transport by the Antilles Current is significantly reduced from 3.4 ± 5.6 Sv in
374 the historical period to -0.72 ± 4.5 Sv in the late 21st century, under SSP-585, with relatively
375 weak variation across scenarios. This suggests that the Antilles Current may turn into a
376 southward current after around 2080 (Fig. 8c). This weakening (and the reversal) of the Antilles
377 Current, which is consistent with a previous modeling study (Cai et al., 2024), may play a key
378 role in the subtropical gyre recirculation and the upper-ocean stratification in the SAB. Fig. 8d
379 shows that volume transport of the Deep Western Boundary Current (DWBC), which is a vital
380 return flow component of the AMOC from the high latitudes, exhibits the strongest response to
381 anthropogenic warming. Particularly under the SSP-585 scenario, the DWBC transport declines
382 from -35.2 ± 9.5 Sv in the historical period to -20.2 ± 16.0 Sv in the late 21st century (42.7 %
383 decline), reflecting a substantial slowdown in the AMOC under SSP-585. This slowdown is once
384 again mitigated in part by intermediate and low emissions scenarios.

385 As was the case for SST, SSS and current speed, the rate of weakening was not very sensitive
386 to the emission scenarios before the 2070s. The insensitivity of Northwestern Atlantic WBCs to
387 emission scenarios before 2070s is highly consistent with AMOC decline patterns in GFDL-
388 ESM4.1 (Supplementary Fig. S6). Previous studies (e.g., Weijer et al., 2020; Baker et al., 2023)



389 found that the rate of AMOC weakening derived from most CMIP6 models shows limited
390 sensitivity to emission scenarios, consistent with GFDL-ESM4.1 prior to 2070. One possible
391 explanation is a time lag in the AMOC response to the inter-scenario difference in the
392 greenhouse gas forcing.

393

394 3.2.3. Dynamic SSH

395 We next explore dynamic SSH and its projected changes under four SSP scenarios (Fig. 9).
396 The substantial changes in both the amplitude and spatial pattern of dynamic SSH are projected
397 in the Northwestern Atlantic. In particular, dynamic SSH increases greatly along the West
398 Florida Shelf (WFS), SAB, MAB, and Georges Bank, and decreases immediately south of the
399 Gulf Stream (after its separation from the US East Coast) under all four SSP scenarios. Given
400 that these changes are largely confined to the region of WBCs and the southern recirculation (or
401 Worthington) gyre south of the Gulf Stream, the dynamic SSH changes appear to be directly
402 linked to the substantial weakening of the WBC system (e.g., the Loop Current, the Florida
403 Current, and the Gulf Stream) and the implied relaxation of the thermocline slope (i.e., a
404 redistribution of mass) across the WBCs. Thus, the projected increases in dynamic SSH along
405 the WFS, SAB, MAB, and the Georges Bank appear to be ultimately driven by the AMOC
406 weakening (e.g., Yin et al., 2009; Little et al., 2017; Weijer et al., 2020). Consistent with
407 MOM6-NWA12, GFDL-ESM4.1 shows an increase in dynamic SSH near the U.S. East Coast
408 and decreases south of the Gulf Stream (after its separation from the US East Coast) in the late
409 21st century (Supplementary Fig. S7). An interesting point to note is that MOM6-NWA12
410 projects a stronger SSH increase in the SAB than in the MAB while GFDL-ESM4.1 projects a
411 stronger SSH increase north of Cape Hatteras than in the south. Consistent with this result, Li et



412 al. (2022) show that the projected SSH derived from a high-resolution Community Earth System
413 Model (CESM) increases more in the SAB than in the MAB, while that derived from a low-
414 resolution CESM increases more in the MAB than in the SAB.

415 To further explore the future increases in dynamic SSH along the US South and East Coasts,
416 we examine the projected dynamic SSH changes over the continental shelf (i.e., depths < 200m)
417 for five sub-regions, namely the Northern GoA, WFS, SAB, MAB, and Gulf of Maine, as shown
418 in Fig. 10. The future increase in dynamic SSH is relatively modest in the Northern GoA and
419 WFS, ranging between 5 and 7 cm during the mid- and late-21st century (2041-2100). These
420 increases occur mainly during the mid-21st century (2041-2060), after which there is no
421 significant increase in the dynamic SSH in these shelf regions. Another important feature is that
422 the dynamic SSH increases in the GoA and WFS (Figs. 10a-b) are not sensitive to the emission
423 scenarios considered. Given that the dynamic SSH increase in these regions is mainly driven by
424 the projected weakening of the AMOC and the associated Loop Current, this result appears to be
425 consistent with the insensitivity in the rate of AMOC's future weakening to the emission
426 scenarios prior to 2070 (Supplementary Fig. S6).

427 In contrast to the Northern GoA and WFS, the projected dynamic SSH changes in the US
428 East Coast shelf regions (i.e., SAB, MAB, and Gulf of Maine) are significantly larger, ranging
429 between 10 and 20 cm in the late-21st century. Additionally, unlike the US GoA shelf regions
430 (i.e., Northern GoA and WFS), the increase in dynamic SSH in these regions continues beyond
431 the mid-21st century to the late-21st century, implying that the weakening of the AMOC and the
432 associated WBCs have much tighter control over these regions. A systematic tendency toward
433 greater dynamic SSH changes in higher emissions scenarios also begins to emerge, though there
434 is still significant variation around this trend (e.g., SSP-370 has a lower local dynamic sea level



435 change than SSP245 despite having higher emissions), presumably due to internal climate
436 variability.

437 Among the five sub-regions considered, the dynamic SSH change in the SAB is subject to
438 the largest increase. The dynamic SSH in the SAB is projected to increase dramatically after
439 around 2040, reaching close to 20 cm in the late 21st century compared to that in the historical
440 period. This suggests that the SAB is the most sensitive to the projected slowdown of the AMOC
441 and the WBCs in MOM6-NWA12. Specifically, as shown in Fig. 11, a strong negative
442 correlation exists between the Florida Current transport and the SAB dynamic SSH (e.g., Ezer,
443 2019; Ezer and Atkinson, 2014) indicating that a -1 Sv reduction in the Florida Current transport
444 corresponds to about 1.7 cm of dynamic SSH increase in the SAB. This indicates that the SAB is
445 the future dynamic SSH rise hotspot, potentially posing an increasing flooding risk in the coastal
446 communities. This appears to be partly due to close proximity of the SAB to the WBC (i.e.,
447 Florida Current in this case). In the other subregions, the shelf area is too far away from the
448 WBC (Northern GoA), too wide (WFS), or mediated by the slope water (MAB and Gulf of
449 Maine).

450 To better understand the relationship between the SAB dynamic SSH increase and the Gulf
451 Stream weakening, we show the vertical profile of ocean temperature and salinity across 26.5°N
452 during the historical period and their projected changes under the four SSP scenarios (Fig. 12).
453 Fig. 12 clearly illustrates a substantial warming and an increase in salinity, mainly along the
454 continental slope and shelf. Due to reduced bottom Ekman transport and the geostrophic
455 adjustment associated with a weakened Gulf Stream, upwelling decreases along the continental
456 slope and shelf, limiting the supply of cold and relatively fresh subsurface water from underneath
457 the Gulf Stream. This indicates that the warm and salty Gulf Stream water penetrates deeper into



458 the continental slope and shelf region due to the weakening of the Gulf Stream. This mass
459 redistribution from the open ocean to the coastal region is also directly responsible for the large
460 projected increase in dynamic SSH across the SAB, which is consistent with the historical
461 analysis of Steinberg et al. (2024).

462 These future changes in ocean conditions near the coastline are also projected in West
463 Florida. The reduction of the Loop Current leads to an increase in dynamic SSH across West
464 Florida and a significant reduction in the upwelling of cold and relatively fresh subsurface water.
465 This, in turn, results in warm, salty Loop Current water penetrating deeper into the WFS (Fig.
466 13).

467 In the MAB (30°N – 41°N , 76°W – 67°W), the weakening and shoreward shift of the Gulf
468 Stream in the late 21st century drives an increase in ocean temperature and salinity along the
469 continental slope and shelf. The maximum SSH anomaly is observed near the core location of
470 the shifted Gulf Stream. Specifically, projected SSH increases on the coastal side of the current
471 while decreasing on the open-ocean side. This differential change results in a reduced cross-
472 stream SSH gradient (slope), consistent with the geostrophic weakening of the flow.

473 Finally, we emphasize that the dynamical changes in SSH described here would occur in
474 addition to static sea level rise associated with basin-scale warming and glacial and ice-sheet
475 melt. As described in the methods, these contributions are not directly reflected in the simulation
476 due to the Boussinesq approximation. Prior analysis, however, suggests static increases between
477 18 – 34 cm over the next century with strong separation between SSP scenarios (e.g., Hermans et
478 al., 2021; Jin et al., 2025).

479

480 **4. Summary and Discussion**



481 This study describes and evaluates the dynamically downscaled physics-only MOM6-
482 NWA12 simulations of GFDL-ESM4, and then explores future changes of the Northwest
483 Atlantic Ocean under four CMIP6 emission scenarios (SSP-126, SSP-245, SSP-370, and SSP-
484 585). Validation of model outputs against direct ocean observational and reanalysis data shows
485 that the biases in GFDL-ESM4 are significantly reduced in MOM6-NWA12, particularly in the
486 spatial SST and SSS patterns, as well as the Gulf Stream's path and volume transport. For
487 instance, while GFDL-ESM4 exhibits pronounced warm and high salinity biases along the US
488 East Coast and a northward shift of the Gulf Stream, MOM6-NWA12 simulates improved
489 representation of these key features, including a better alignment of the Gulf Stream path with
490 observations. Furthermore, MOM6-NWA12 captures the spatial pattern of SSH much more
491 accurately, as well as the WBCs (i.e., Florida Current, Yucatan Current, Antilles Current, and
492 DWBC).

493 The projections derived from MOM6-NWA12 show significant changes in SST, SSS and the
494 WBCs under the four SSP scenarios considered. The magnitude of end-of-century changes is
495 strongly scenario-dependent: pronounced SST warming in the MAB and Gulf of Maine,
496 exceeding 4°C in some areas, emerges as a distinct feature of the prior “worst-case” high-
497 emission scenarios (SSP-585), partial mitigation is apparent in intermediate trajectories more
498 consistent with current CO₂ trajectories (SSP-370, SSP-245), and this signal remains modest
499 under low-emission scenarios (SSP-126). The amplified warming along the US South and East
500 Coasts appears to be linked to a weakening of the Loop Current and Gulf Stream (e.g., Liu et al.,
501 2012, 2015; Saba et al., 2016) alongside a shoreward and northward shift of the Gulf Stream
502 following its separation from the coast (e.g., Yin et al., 2009; Saba et al., 2016; Bellomo et al.,
503 2021; Li et al., 2022). A consistent feature across all projections is the significant deceleration of



504 the surface speed and volume transport of the four WBCs (i.e., Yucatan Current, Florida Current,
505 Antilles Current and DWBC), which aligns well with the significant weakening of the AMOC.
506 Reductions in the meridional transports of the four WBCs remain insensitive to emission
507 scenarios until the 2070s, after which they diverge significantly (ranging from ~23% in SSP-126
508 to ~38% in SSP-585 scenarios).

509 The projections also suggest that the slowdown of the WBCs leads to an increase in dynamic
510 SSH along the US South and East Coasts, which is largest in the SAB. The increased dynamic
511 SSH in these regions is directly related to the weakening of the WBCs and the associated
512 redistribution of the mass across the WBCs (Minobe et al., 2017). As such, a strong negative
513 correlation exists between the Florida Current transport and the dynamic SSH in the SAB, for
514 example. Further analysis indicates that the weakening of the Florida Current accompanies a
515 substantial reduction of upwelling of cold and fresh subsurface water to the continental slope and
516 shelf region. The associated decrease in nutrient supply, implied by the reduced upwelling, has
517 important implications for the marine ecosystems and productivity in the SAB, as the Gulf
518 Stream-induced upwelling represents the main source of nutrients to the SAB outer and mid shelf
519 (e.g., Lee et al., 1991).

520 While this study has mostly focused on describing the future mean changes across scenarios,
521 there are several areas that require further investigation, such as the changes in the seasonal
522 circulation patterns and their impact on the anomalous ocean conditions. This could be relevant,
523 for example, in the MAB where seasonal changes in wind stress drives the annual sea level
524 height variability (e.g., Yang and Chen, 2025). It could also be relevant for the SAB where the
525 seasonal wind stress changes impact coastal temperature and cross-shore interchanges through



526 upwelling (e.g., Castelao et al., 2011; Yuan et al., 2017). Therefore, further study is needed to
527 explore future changes in the seasonality of WBCs, and their impacts.

528 Lastly, building on these results derived from physics-only simulations, we plan to couple the
529 physical ocean model with the Carbon, Ocean Biogeochemistry and Lower Trophics (COBALT,
530 Stock et al., 2020, 2025) model to explore future changes in ocean ecosystems in the Northwest
531 Atlantic. Additionally, we will expand the scenario-focused ensemble presented here to include
532 multiple GCMs to fully assess the potential range of the future changes in the Northwest
533 Atlantic.

534

535 **Acknowledgements**

536 This study was supported by the NOAA's Changing Ecosystems, and Fisheries Initiative
537 (CEFI) and the NOAA award Number NA24OARX405C0044-T1-01. This study was also
538 carried out under the auspices of the Cooperative Institute for Marine and Atmospheric Studies
539 (CIMAS) (NOAA cooperative agreement NA20OAR4320472), the Northern Gulf Institute
540 (NGI) (NOAA cooperative agreement NA21OAR4320190), and supported by NOAA's Oceanic
541 and Atmospheric Research and NOAA's Atlantic Oceanographic and Meteorological
542 Laboratory.

543

544 **Code availability**

545 The source code for each component of the MOM6-NWA12 model has been archived by
546 Ross et al. (2023) and the GitHub repositories are located at [https://github.com/NOAA-](https://github.com/NOAA-GFDL/CEFI-regional-MOM6)
547 [GFDL/CEFI-regional-MOM6](https://github.com/NOAA-GFDL/CEFI-regional-MOM6). All codes for analyses were performed using the Grid Analysis
548 and Display System (GrADS), which is publicly available from the Center for Ocean-Land-



549 Atmosphere Studies at <http://cola.gmu.edu/grads> and NCL, which is publicly available from the
550 NCAR Command Language (NCL) at <https://www.ncl.ucar.edu/>. The GrADS, NCL, and Fortran
551 codes used to perform the analyses can be accessed upon request to D. K.

552

553 **Data availability**

554 The model outputs derived from the MOM6-NWA12 future projections under four SSP
555 scenarios will be available at CEFI portal soon (https://psl.noaa.gov/cefi_portal/). GLORYS12
556 reanalysis dataset is available at <https://data.marine.copernicus.eu/product/>. ERA5 reanalysis
557 dataset is available at <https://cds.climate.copernicus.eu/datasets/reanalysis-era5-single-levels>.
558 GFDL-ESM4 outputs are freely available at the CMIP6 archive
559 (<https://aims2.llnl.gov/search/cmip6/>).

560

561 **Author Contribution**

562 D Kim, AC Ross, SI Shin and SK Lee contributed source code for downscaling system for the
563 regional MOM6. D Kim, SI Shin and SK Lee contributed to preparation of model input files. D
564 Kim, FA Gomez and SK Lee contributed to evaluation and interpretation of the model results. D
565 Kim and SK Lee prepared the initial draft of manuscript. All coauthors participated in
566 discussions during various stages of the model development and evaluation and read and
567 approved the final version of the manuscript.

568

569 **Competing interests**

570 Dr. Charles A. Stock (one of co-authors) serves as editor for the special issue to which this paper
571 belongs.



572 **References**

573 1. Adcroft, A., Anderson, W., Balaji, V., Blanton, C., Bushuk, M., Dufour, C. O., Dunne, J. P.,
574 Griffies, S. M., Hallberg, R., Harrison, M. J., Held, I. M., Jansen, M. F., John, J. G., Krasting,
575 J. P., Langenhorst, A. R., Legg, S., Liang, Z., McHugh, C., Radhakrishnan, A., Reichl, B. G.,
576 Rosati, T., Samuels, B. L., Shao, A., Stouffer, R., Winton, M., Wittenberg, A. T., Xiang, B.,
577 Zadeh, N., and Zhang, R.: The GFDL Global Ocean and Sea Ice Model OM4.0: Model
578 Description and Simulation Features, *Journal of Advances in Modeling Earth Systems*, 11,
579 3167–3211, <https://doi.org/10.1029/2019MS001726>, 2019.

580 2. Adcroft, A., and Campin, J.-M.: Rescaled height coordinates for accurate representation of
581 free-surface flows in ocean circulation models, *Ocean Modelling*, 7, 269–284,
582 <https://doi.org/10.1016/j.ocemod.2003.09.003>, 2004.

583 3. Adcroft, A., and Hallberg, R.: On methods for solving the oceanic equations of motion in
584 generalized vertical coordinates, *Ocean Modelling*, 11, 224–233,
585 <https://doi.org/10.1016/j.ocemod.2004.12.007>, 2006

586 4. Alexander, M. A., and Scott, J. D.: The Role of Ekman Ocean Heat Transport in the Northern
587 Hemisphere Response to ENSO, *Journal of Climate*, 21, 5688–5707,
588 <https://doi.org/10.1175/2008JCLI2382.1>, 2008.

589 5. Alexander, M. A., Shin, S., Scott, J. D., Curchitser, E., and Stock, C.: The Response of the
590 Northwest Atlantic Ocean to Climate Change, *Journal of Climate*, 33, 405–428,
591 <https://doi.org/10.1175/JCLI-D-19-0117.1>, 2020.

592 6. Alfieri, L., Lorini, V., Hirpa, F. A., Harrigan, S., Zsoter, E., Prudhomme, C., and Salamon,
593 P.: A Global Streamflow Reanalysis for 1980–2018, *Journal of Hydrology*, 6, 100049,
594 <https://doi.org/10.1016/j.jhydro.2019.100049>, 2020.



595 7. Athié, G., Sheinbaum, J., Leben, R., Ochoa, J., Shannon, M. R., and Candela, J.: Interannual
596 variability in the Yucatan Channel flow, *Geophysical Research Letters*, 42, 1496–1503,
597 doi:10.1002/2014GL062674, 2015.

598 8. Baker, J. A., Bell, M. J., Jackson, L. C., Renshaw, R., Vallis, G. K., Watson, A. J., and Wood,
599 R. A.: Overturning pathways control AMOC weakening in CMIP6 models. *Geophysical
600 Research Letters*, 50, e2023GL103381. https://doi.org/10.1029/2023GL103381, 2023.

601 9. Bell, R. J., Richardson, D. E., Hare, J. A., Lynch, P. D., and Fratantoni, P. S.: Disentangling
602 the effects of climate, abundance, and size on the distribution of marine fish: an example
603 based on four stocks from the Northeast US shelf, *ICES Journal of Marine Science*, 72,
604 1311–1322, https://doi.org/10.1093/icesjms/fsu217, 2015.

605 10. Bellomo, K., Angeloni, M., Corti, S. and Hardenberg, J.: Future climate change shaped by
606 inter-model differences in Atlantic meridional overturning circulation response, *Nature
607 Communications*, 12, 3659, https://doi.org/10.1038/s41467-021-24015-w, 2021.

608 11. Caesar, L., Rahmstorf, S., Robinson, Feulner, G., and Saba, V.: Observed fingerprint of a
609 weakening Atlantic Ocean overturning circulation, *Nature*, 556, 191–196,
610 https://doi.org/10.1038/s41586-018-0006-5, 2018.

611 12. Cai, J., Yang, H., Chen, Z., and Wu, L.: The disappearing Antilles Current dominates the
612 weakening meridional heat transport in the North Atlantic Ocean under global warming,
613 *Environmental Research Letters*, 19, 044049, https://doi.org/10.1088/1748-9326/ad3567,
614 2024.

615 13. Castelao, R.: Intrusions of Gulf Stream waters onto the South Atlantic Bight shelf, *Journal of
616 Geophysical Research: Oceans*, 116, C10011, https://doi.org/10.1029/2011JC007178, 2011.



617 14. Chassignet, E., and Marshall. D.: Gulf Stream separation in numerical ocean models, In
618 Ocean Modeling in an Eddying Regime, Geophysical Monograph Series, 177, 2008.

619 15. Cheng, C. S., Li, G., Li, Q., Auld, H., and Fu, C.: Possible Impacts of Climate Change on
620 Wind Gusts under Downscaled Future Climate Conditions over Ontario, Canada, Journal of
621 Climate, 25, 3390–3408, <https://doi.org/10.1175/JCLI-D-11-00198.1>, 2012.

622 16. Dong, S., Baringer, M., and Goni, G.: Slowdown of the Gulf Stream during 1993–2016.
623 Scientific Reports, 9, 6672, <https://doi.org/10.1038/s41598-019-42820-8>, 2019.

624 17. Domingues, R., Goni, G., Baringer, M., and Volkov, D.: What caused the accelerated sea
625 level changes along the U.S. East Coast during 2010–2015?, Geophysical Research Letters,
626 45, 13367–13376, <https://doi.org/10.1029/2018GL081183>, 2018.

627 18. Drenkard, E. J., Stock, C., Ross, A. C., Dixon, K. W., Adcroft, A., Alexander, M., Balaji, V.,
628 Bograd, S. J., Butenschön, M., Cheng, W., Curchitser, E., Lorenzo, E. D., Dussin, R.,
629 Haynie, A. C., Harrison, M., Hermann, A., Hollowed, A., Holsman, K., Holt, J., Jacox, M.
630 G., Jang, C. J., Kearney, K. A., Muhling, B. A., Buil, M. P., Saba, V., Sandø, A. B.,
631 Tommasi, D., and Wang, M.: Next-generation regional ocean projections for living marine
632 resource management in a changing climate, ICES Journal of Marine Science, 78, 1969–
633 1987, <https://doi.org/10.1093/icesjms/fsab100>, 2021.

634 19. Dunne, J. P., Horowitz, L. W., Adcroft, A. J., Ginoux, P., Held, I. M., John, J. G., Krasting, J.
635 P., Malyshev, S., Naik, V., Paulot, F., Shevliakova, E., Stock, C. A., Zadeh, N., Balaji, V.,
636 Blanton, C., Dunne, K. A., Dupuis, C., Durachta, J., Dussin, R., Gauthier, P. P. G., Griffies,
637 S. M., Guo, H., Hallberg, R. W., Harrison, M., He, J., Hurlin, W., McHugh, C., Menzel, R.,
638 Milly, P. C. D., Nikonorov, S., Paynter, D. J., Poshay, J., Radhakrishnan, A., Rand, K., Reichl,
639 B. G., Robinson, T., Schwarzkopf, D. M., Sentman, L. T., Underwood, S., Vahlenkamp,



640 H., and Winton, M.: The GFDL Earth SystemModel Version 4.1 (GFDL-ESM 4.1): Overall
641 coupled model description and simulation characteristic, *Journal of Advances in Modeling*
642 *Earth Systems*, 12, e2019MS002015. <https://doi.org/10.1029/2019MS002015>, 2020.

643 20. Ezer, T.: Detecting changes in the transport of the Gulf Stream and the Atlantic overturning
644 circulation from coastal sea level data: The extreme decline in 2009–2010 and estimated
645 variations for 1935–2012, *Global and Planetary Change*, 129, 23–36.
646 <https://doi.org/10.1016/j.gloplacha.2015.03.002>, 2015.

647 21. Ezer, T.: Regional differences in sea level rise between the Mid-Atlantic Bight and the South
648 Atlantic Bight: Is the Gulf Stream to blame?, *Earth's Future*, 7, 771–783.
649 <https://doi.org/10.1029/2019EF001174>, 2019.

650 22. Ezer, T., and Atkinson, L. P.: Accelerated flooding along the U.S. EastCoast: On the impact
651 of sea-level rise,tides, storms, the Gulf Stream, and the North Atlantic Oscillations, *Earth's
652 Future*, 2, 362–382,doi:10.1002/2014EF000252, 2014.

653 23. Ezer, T., Atkinson, L. P., Corlett, W. B., and Blanco, J. L.: Gulf Stream's induced sea level
654 rise and variability along the US mid-Atlantic coast, *Journal of Geophysical Research:
655 Oceans*, 118, 685–697, <https://doi.org/10.1002/jgrc.20091>, 2013.

656 24. Friedrichs, M. A. M., St-Laurent, P., Xiao, Y., Hofmann, E., Hyde, K., Mannino, A., Najjar,
657 R. G., Narváez, D. A., Signorini, S.R., Tian, H., Wilkin, J., Yao, Y., Xue, J.: Ocean
658 circulation causes strong variability in the Mid-Atlantic Bight nitrogen budget. *Journal of
659 Geophysical Research: Oceans*, 124, 113–134. <https://doi.org/10.1029/2018JC014424>, 2019.

660 25. Giuntoli, I., Vidal, J.-P, Prudhomme, C., and Hannah, D.M.: Future hydrological extremes:
661 the uncertainty from multiple global climate and global hydrological models, *Earth System
662 Dynamics*, 6, 267–285, 2015.



663 26. Goddard, P. B., Yin, J., Griffies, S. M., and Zhang, S.: An extreme event of sea-level rise
664 along the Northeast coast of North America in 2009–2010, *Nature Communications*, 6,
665 <https://doi.org/10.1038/ncomms7346>, 2015.

666 27. Gomez, F.A., Lee, S.K., Hernandez, F.J., Chiaverano, L.M., Muller-Karger, F.E., Liu, Y.,
667 and Lamkin, J.T.: ENSO-induced co-variability of Salinity, Plankton Biomass and Coastal
668 Currents in the Northern Gulf of Mexico. *Scientific reports*, 9, 178,
669 <https://doi.org/10.1038/s41598-018-36655-y>, 2019.

670 28. Gomez, F. A., Lee, S.-K., Stock, C. A., Ross, A.C., Resplandy, L., Siedlecki, S.A., Tagklis,
671 F., and Salisbury, J. E.: RC4USCoast: A river chemistry dataset for regional ocean model
672 applications in the U.S. East, Gulf of Mexico, and West Coasts, *Earth System Science Data*,
673 <https://doi.org/10.5194/essd-2022-341>, 2022.

674 29. Gomez, F.A., Wanninkhof, R., Barbero, L., and Lee, S.-K.: Mississippi River Chemistry
675 Impacts on the Interannual Variability of Aragonite Saturation State in the Northern Gulf of
676 Mexico, *Journal of Geophysical Research: Oceans*, 129, e2023JC020436, 2024.

677 30. Gomez, F.A., Wanninkhof, R., Barbero, L., Lee, S.K., and Hernandez, F. J.: Seasonal
678 patterns of surface inorganic carbon system variables in the Gulf of Mexico inferred from a
679 regional high-resolution ocean biogeochemical model, *Biogeosciences*, 17, 1685–1700.
680 <https://doi.org/10.5194/bg-17-1685-2020>, 2020.

681 31. Greatbatch, R. J.: A note on the representation of steric sea level in models that conserve
682 volume rather than mass. *Journal of Geophysical Research: Oceans*, 12, 767–12,771, 1994.

683 32. Griffies, S. M., and Greatbatch, R. J.: Physical processes that impact the evolution of global
684 mean sea level in ocean climate models, *Ocean Modelling*, 51, 37–72, 2012.



685 33. Griffies, S. M., Yin, J., Durack, P. J., Goddard, P., Bates, S. C., Behrens, E., Bentsen, M., Bi,
686 D., Biastoch, A., Böning, C., Bozec, A., Chassignet, E., Danabasoglu, G., Danilov, S.,
687 Domingues, C. M., Drange, H., Farneti, R., Fernandez, E., Greatebatch, R. J., Holland, D.
688 M., Ilicak, M., Large, W. G., Lorbacher, K., Lu, J., Marsland, S. J., Mishra, A., Nurser, A. J.
689 G., Salas y Mélia, D., Palter, J. B., Samuels, B. L., Schröter, Schwarzkopf, F. U., Sidorenko,
690 D., Treguier, A.-M., Tseng, Y. H., Tsujino, H., Uotila, P., Valcke, S., Voldoire, A., Wang,
691 Q., Winton, M., and Zhang, X.: An assessment of global and regional sea level for years
692 1993–2007 in a suite of interannual CORE-II simulations, *Ocean Modelling*, 78, 35–89,
693 <https://doi.org/10.1016/j.ocemod.2014.03.004>, 2014.

694 34. Hameed, S., C. Wolfe, L. P., and Chi, L.: Impact of the Atlantic Meridional Mode on Gulf
695 Stream North Wall Position, *Journal of Climate*, 31, 8875–8894,
696 <https://doi.org/10.1175/JCLI-D-18-0098.1>, 2018.

697 35. Hermans, T. H. J., Gregory, J. M., Palmer, M. D., Ringer, M. A., Katsman, C. A., and
698 Slangen, A. B. A.: Projecting global mean sea-level change using CMIP6 models,
699 *Geophysical Research Letters*, 48, e2020GL092064. <https://doi.org/10.1029/2020GL092064>,
700 2021.

701 36. Hersbach, H., Bell, B., Berrisford, P., Hirahara, S., Horányi, A., Muñoz-Sabater, J., Nicolas,
702 J., Peubey, C., Radu, R., Schepers, D., Simmons, A., Soci, C., Abdalla, S., Abellan, X.,
703 Balsamo, G., Bechtold, P., Biavati, G., Bidlot, J., Bonavita, M., De Chiara, G., Dahlgren, P.,
704 Dee, D., Diamantakis, M., Dragani, R., Flemming, J., Forbes, R., Fuentes, M., Geer, A.,
705 Haimberger, L., Healy, S., Hogan, R. J., Hólm, E., Janisková, M., Keeley, S., Laloyaux, P.,
706 Lopez, P., Lupu, C., Radnoti, G., de Rosnay, P., Rozum, I., Vamborg, F., Villaume, S., and



707 Thépaut, J.-N.: The ERA5 Global Reanalysis, Quarterly Journal of the Royal Meteorological
708 Society, 146, 1999–2049, <https://doi.org/10.1002/qj.3803>, 2020.

709 37. Huang, L., Volkov, D. L., Dong, S., and Schmid, C.: On the rapid warming in the subtropical
710 North Atlantic in 2011–2021, Geophysical Research Letters, 52, e2025GL116280.
711 <https://doi.org/10.1029/2025GL116280>, 2025.

712 38. Jackson, L. C., and Wood, R. A.: Timescales of AMOC decline in response to fresh water
713 forcing, Climate Dynamics, 51, 1333–1350, 2018.

714 39. Jeong, D.I., and Sushama, L.: Projected Changes to Mean and Extreme Surface Wind Speeds
715 for North America Based on Regional Climate Model Simulations, Atmosphere, 10, 497,
716 <https://doi.org/10.3390/atmos10090497>, 2019.

717 40. Jin, C., Liu, H., Lin, P., Lyu, K., and Li, Y.: Uncertainties in the projection of stereodynamic
718 sea level in CMIP6 models, Geophysical Research Letters, 52, e2024GL113691.
719 <https://doi.org/10.1029/2024GL113691>, 2025.

720 41. Karnauskas, M., Schirripa, M.J., Craig, K., Cook, G., Kelble, C., Agar, J., Black, B., Enfield,
721 D., Lindo-Atichati, D., Muhling, B., Purcell, K., Richards, P., and Wang C. Evidence of
722 climate-driven ecosystem reorganization in the Gulf of Mexico, Global Change Biology, 21,
723 2554–2568, 2015.

724 42. Karnauskas, M., Schirripa, M.J., Kelble, C.K., Cook, G.S., and Craig, J.K.: Ecosystem status
725 report for the Gulf of Mexico, NOAA Technical Memorandum NMFS-SEFSC-653, 2013

726 43. Koul, V., Ross, A. C., Stock, C., Zhang, L., Delworth, T., and Wittenberg, A.: A predicted
727 pause in the rapid warming of the Northwest Atlantic Shelf in the coming decade, Geophysical
728 Research Letters, 51, e2024GL110946, <https://doi.org/10.1029/2024GL110946>, 2024.



729 44. Lee, T. N., Yoder, J. A., and Atkinson, L. P.: Gulf Stream frontal eddy influence on
730 productivity of the 857 southeast US Continental Shelf, *Journal of Geophysical Research: Oceans*, 96, 191–205, <https://doi.org/10.1029/91jc02450>, 1991.

732 45. Lellouche, J., Greiner, E., Bourdallé-Badie, R., Garric, G., Melet, A., Drévillon, M., Bricaud,
733 C., Hamon, M., Le Galloudec, O., Regnier, C., Candela, T., Testut, C., Gasparin, F.,
734 Ruggiero, G., Benkiran, M., Drillet, Y., and Le Traon, P.: The Copernicus Global 1/12
735 Oceanic and Sea Ice GLORYS12 Reanalysis, *Frontiers in Earth Science*, 9, 698876,
736 <https://doi.org/10.3389/feart.2021.698876>, 2021.

737 46. Levermann, A., Griesel, A., Hofmann, M., Montoya, M., and Rahmstorf, S.: Dynamic sea
738 level changes following changes in the thermohaline circulation, *Climate Dynamics*, 24,
739 347–354, <https://doi.org/10.1007/s00382-004-0505-y>, 2005.

740 47. Li, D., Chang, P., Yeager, S. G., Danabasoglu, G., Castruccio, F. S., Small, Wang, H.,
741 Zhang, Q., and Gopal, A.: The impact of horizontal resolution on projected sea-level rise
742 along US east continental shelf with the community earth system model, *Journal of Advances
743 in Modeling Earth Systems*, 14, e2021MS002868, 2022.

744 48. Lin, S. J.: A “vertically Lagrangian” finite-volume dynamical core for global models,
745 *Monthly Weather Review*, 132, 2293–2307. 2004.

746 49. Little, C. M., Hu, A., Hughes, C. W., McCarthy, G. D., Piecuch, C. G., Ponte, R. M., and
747 Thomas, M. D.: The Relationship between U.S. East Coast sea level and the Atlantic
748 Meridional Overturning Circulation: A review, *Journal of Geophysical Research: Oceans*, 124,
749 6435–6458, <https://doi.org/10.1029/2019JC015152>, 2019.

750 50. Little, C. M., Piecuch, C. G., and Ponte, R. M.: On the relationship between the meridional
751 overturning circulation, alongshore wind stress, and United States East Coast sea level in the



752 Community Earth System Model Large Ensemble, *Journal of Geophysical Research: Oceans*
753 122, 4554–4568, <https://doi.org/10.1002/2017JC012713>, 2017.

754 51. Liu, Y., Lee, S.-K., Enfield, D. B., Muhling, B. A., Lamkin, J. T., Muller-Karger, F. E., and
755 Roffer, M. A.: Potential impact of climate change on the Intra-Americas Sea: Part-1. A
756 dynamic downscaling of the CMIP5 model projections, *Journal of Marine Systems*, 148, 56–
757 69, <https://doi.org/10.1016/j.jmarsys.2015.01.007>, 2015.

758 52. Liu, Y., Lee, S.-K., Muhling, B.A., Lamkin, J.T., and Enfield, D.B.: Significant reduction of
759 the Loop Current in the 21st century and its impact on the Gulf of Mexico, *Journal of
760 Geophysical Research: Oceans*, 117, C05039. <http://dx.doi.org/10.1029/2011JC007555>, 2012.

761 53. Meinen, C. S., Johns, W. E., Moat, B. I., Smith, R. H., Johns, E. M., Rayner, D., Frajka-
762 Williams, E., Garcia, R.F., and Garzoli, S. L.: Structure and variability of the Antilles
763 Current at 26.5°N, *Journal of Geophysical Research: Oceans*, 124, 3700–3723.
764 <https://doi.org/10.1029/2018JC014836>, 2019.

765 54. Minobe, S., Terada, M., Qiu, B., and Schneider, N.: Western boundary sea level: A theory,
766 rule of thumb, and application to climate models, *Journal of Physical Oceanography*, 47,
767 957–977, <https://doi.org/10.1175/JPO-D-16-0144.1>., 2017.

768 55. Muller-Karger, F. E., Smith, J. P., Werner, S., Chen, R., Roffer, M., Liu, Y., Muhling, B.,
769 Lindo-Atichati, D., Lamkin, J., Cerdeira-Estrada, S., and Enfield, D. B.: Natural variability of
770 surface oceanographic conditions in the offshore Gulf of Mexico, *Progress in Oceanography*,
771 134, 54–76. 2015.

772 56. O'Neill, B. C., Tebaldi, C., van Vuuren, D. P., Eyring, V., Friedlingstein, P., Hurt, G.,
773 Knutti, R., Kriegler, E., Lamarque, J.-F., Lowe, J., Meehl, G. A., Moss, R., Riahi, K., and
774 Sanderson, B. M.: The Scenario Model Intercomparison Project (ScenarioMIP) for CMIP6,



775 Geoscientific Model Development, 9, 3461–3482, <https://doi.org/10.5194/gmd-9-3461-2016>,
776 2016.

777 57. Park, J., and Sweet, W.: Accelerated sea level rise and Florida Current transport. *Ocean*
778 *Science*, 11, 607–615. <https://doi.org/10.5194/os-11-607-2015>, 2015.

779 58. Pershing A. J., Alexander M. A., Hernandez C. M., Kerr L. A., Le Bris A., Mills K. E., Nye
780 J. A., Record N. R., Scannell H. A., Scott J. D., Sherwood G. D., and Thomas A. C.: Slow
781 adaptation in the face of rapid warming leads to collapse of the Gulf of Maine cod fishery,
782 *Science*, 350, 809–812, 2015.

783 59. Pozo Buil M., Jacox, M. G., Fiechter, J., Alexander, M.A., Bograd, S.J., Curchitser, E.N.,
784 Edwards, C.A., Rykaczewski, R.R., and Stock, C.A.: A Dynamically Downscaled Ensemble
785 of Future Projections for the California Current System, *Frontiers Marine Sciences*,
786 8:612874, doi: 10.3389/fmars.2021.612874, 2021.

787 60. Ross, A. C., Stock, C. A., Adcroft, A., Curchitser, E., Hallberg, R., Harrison, M. J.,
788 Hedstrom, K., Zadeh, N., Alexander, M., Chen, W., Drenkard, E. J., du Pontavice, H.,
789 Dussin, R., Gomez, F., John, J. G., Kang, D., Lavoie, D., Resplandy, L., Roobaert, A., Saba,
790 V., Shin, S.-I., Siedlecki, S., and Simkins, J.: A high-resolution physical–biogeochemical
791 model for marine resource applications in the northwest Atlantic (MOM6-COBALT-NWA12
792 v1.0), *Geoscientific Model Development*, 16, 6943–6985, <https://doi.org/10.5194/gmd-16-6943-2023>, 2023.

794 61. Ross, A. C., Stock, C. A., Koul, V., Delworth, T. L., Lu, F., Wittenberg, A., and Alexander,
795 M. A.: Dynamically downscaled seasonal ocean forecasts for North American east coast
796 ecosystems, *Ocean Science*, 20, 1631–1656, <https://doi.org/10.5194/os-20-1631-2024>, 2024.



797 62. Rutherford, K., Fennel, K., Garcia Suarez, L., and John, J. G.: Uncertainty in the evolution of
798 northwestern North Atlantic circulation leads to diverging biogeochemical projections,
799 Biogeosciences, 21, 301–314, <https://doi.org/10.5194/bg-21-301-2024>, 2024.

800 63. Saba, V. S., Griffies, S. M., Anderson, W. G., Winton, M., Alexander, M. A., Delworth, T.
801 L., Hare J.A., Harrison M. J., Rosati A., Vecchi G. A., and Zhang, R.: Enhanced warming of
802 the Northwest Atlantic Ocean under climate change, Journal of Geophysical Research:
803 Oceans, 121, 118-132, 2016.

804 64. Sanchez-Franks, A., and Zhang, J.: Decadal variability and shifts of the Gulf Stream path,
805 Journal of Climate, 28, 9825-9838, 2015.

806 65. Seidov, D., Gilman, C., and Haupt, B. J.: Global Ocean Circulation: A Review of the Current
807 State of Knowledge, Atmosphere, 10, 446, 2019.

808 66. Shevliakova, E., Malyshev, S., Martinez-Cano, I., Milly, P. C. D., Pacala, S. W.,Ginoux, P.,
809 Dunne, K. A., Dunne, J. P., Dupuis, C., Findell, K. L., Ghannam, K., Horowitz, L. W.,
810 Knutson, T. R., Krasting, J. P., Naik, V., Phillipps, P., Zadeh, N., Yu, Y., Zeng, F., and
811 Zeng, Y.: The land component LM4.1 of the GFDL Earth System Model ESM4.1: Model
812 description and characteristics of land surface climate and carbon cycling in the historical
813 simulation, Journal of Advances in Modeling Earth Systems, 16, e2023MS003922.
814 <https://doi.org/10.1029/2023MS003922>, 2024.

815 67. Shin, S., and Alexander, M. A.: Dynamical Downscaling of Future Hydrographic Changes
816 over the Northwest Atlantic Ocean, Journal of Climate, 33, 2871–2890,
817 <https://doi.org/10.1175/JCLI-D-19-0483.1>, 2020.

818 68. Steinberg, J. M., Griffies, S. M., Krasting, J. P., Piecuch, C. G., and Ross, A. C.: A Link
819 between U.S. East coast sea level and North Atlantic subtropical ocean heatcontent, Journal



820 of Geophysical Research:Oceans, 129, e2024JC021425.

821 <https://doi.org/10.1029/2024JC021425>, 2024.

822 69. Stock, C. A., Dunne, J. P., Fan, S., Ginoux, P., John, J., Krasting, J. P., Laufkötter, C.,

823 Paulot, F., and Zadeh, N.: Ocean Biogeochemistry in GFDL's Earth System Model 4.1 and

824 Its Response to Increasing Atmospheric CO₂, J. Adv. Model. Earth Sy., 12,

825 e2019MS002043, <https://doi.org/10.1029/2019MS002043>, 2020.

826 70. Stock, C. A., Dunne, J. P., Luo, J. Y., Ross, A. C., Van Oostende, N., Zadeh, N., Cordero, T.

827 J., Liu, X., Teng Y-C.: Photoacclimation and photoadaptation sensitivity in a global ocean

828 ecosystem model, Journal of Advances in Modeling Earth Systems, 17, e2024MS004701.

829 <https://doi.org/10.1029/2024MS004701>, 2025.

830 71. Tanaka, K. R., Torre, M. P., Saba, V. S., Stock, C. A., and Chen, Y.: An ensemble high-

831 resolution projection of changes in the future habitat of American lobster and sea scallop in

832 the Northeast US continental shelf, Diversity and Distributions, 26, 987–1001,

833 <https://doi.org/10.1111/ddi.13069>, 2020.

834 72. Volkov, D. L., Lee, S.-K., Domingues, R., Zhang, H., and Goes, M.: Interannual sea level

835 variability along the southeastern seaboard of the United States in relation to whom it may

836 concern: The gyre-scale heat divergence in the North Atlantic, Geophysical Research Letters,

837 46, 7481–7490. <https://doi.org/10.1029/2019GL083596>, 2019.

838 73. Volkov, D.L., Smith, R.H., Garcia, R.F., Smeed, D. A., Moat, B. I., Johns, W. E., and

839 Baringer, M. O.: Florida Current transport observations reveal four decades of steady state,

840 Nature Communications, 15, 7780, <https://doi.org/10.1038/s41467-024-51879-5>, 2024.

841 74. Volkov, D.L., Zhang, K., Johns, W.E. Willis, J. K., Hobbs, W., Goes, M., Zhang, H., and

842 Menemenlis, D.: Atlantic meridional overturning circulation increases flood risk along the



843 United States southeast coast, *Nature Communications*, 14, 5095,

844 <https://doi.org/10.1038/s41467-023-40848-z>, 2023.

845 75. Wang, Z., Boyer, T., Reagan, J., and Hogan, P.: Upper-Oceanic Warming in the Gulf of

846 Mexico between 1950 and 2020, *Journal of Climate*, 36, 2721–2734,

847 <https://doi.org/10.1175/JCLI-D-22-0409.1>, 2023.

848 76. Wang, Z. A., Wanninkhof, R., Cai, W.-J., Byrne, R. H., Hu, X., Peng, T.-H., and Huang, W.-

849 J.: The marine inorganic carbon system along the Gulf of Mexico and Atlantic coasts of the

850 United States: Insights from a transregional coastal carbon study, *Limnology and*

851 *Oceanography*, 58, 325–342, 2013.

852 77. Wanninkhof, R., Barbero, L., Byrne, R., Cai, W.-J., Zhang, H. Z., Baringer, M., and

853 Langdon, C.: Ocean acidification along the Gulf Coast and East Coast of the USA,

854 *Continental Shelf Research*, 98, 54–71. 2015.

855 78. Weijer, W., Cheng, W., Garuba, O. A., Hu, A., and Nadiga, B. T.: CMIP6 models predict

856 significant 21st century decline of the Atlantic Meridional Overturning Circulation,

857 *Geophysical Research Letters*, 47, e2019GL086075. <https://doi.org/10.1029/2019GL086075>,

858 2020.

859 79. Weinberg, J. R.: Bathymetric shift in the distribution of Atlantic surfclams: response to

860 warmer ocean temperature, *ICES Journal of Marine Science*, 62, 1444–1453,

861 <https://doi.org/10.1016/j.icesjms.2005.04.020>, 2005.

862 80. Worthington, L. V.: On the north Atlantic circulation, *John Hopkins Oceanographic Studies*,

863 6, 110, 1976.



864 81. Yang, J., and Chen, K.: Profound changes in the seasonal cycle of sea level along the United
865 States Mid-Atlantic Coast. *Geophysical Research Letters*, 52, e2024GL112273.
866 <https://doi.org/10.1029/2024GL112273>, 2025.

867 82. Yin, J., Schlesinger, M. and Stouffer, R.: Model projections of rapid sea-level rise on the
868 northeast coast of the United States. *Nature Geosciences*, 2, 262–266,
869 <https://doi.org/10.1038/ngeo462>, 2009.

870 83. Yuan, Y., Castelao, R.M. and He, R.: Variability in along-shelf and cross-shelf circulation in
871 the South Atlantic Bight, *Continental Shelf Research*, 134, 52-62,
872 <https://doi.org/10.1016/j.csr.2017.01.006>, 2017.

873 84. Zantopp, R., Fischer, J., Visbeck, M., and Karstensen, J.: From interannual to decadal: 17
874 years of boundary current transports at the exit of the Labrador Sea, *Journal of Geophysical
875 Research: Oceans*, 122, 1724–1748, doi:10.1002/2016JC012271, 2017.

876 85. Zhang, W., Alatalo, P., Crockford, T., Hirzel, A.J., Meyer, M.G., Oliver, H., Peacock, E.,
877 Petitpas, C.M., Sandwith, Z., Smith, W.O., Sosik, H.M., Stanley, R.H.R., Stevens, B.L.F.,
878 Turner, J.T., and McGillicuddy, D.J.: Cross-shelf exchange associated with a shelf-water
879 streamer at the Mid-Atlantic Bight shelf edge. *Progress in Oceanography*, 210, 102931, 2023.

880 86. Zhao, M., Golaz, J.-C., Held, I. M., Guo, H., Balaji, V., Benson, R., Chen, J. H., Chen, X.,
881 Donner, L. J., Dunne, J., Dunne, K. A., Durachta, J., Fan, S.-M., Freidenreich, S. M., Garner,
882 S. T., Ginoux, P., Harris, L., Horowitz, L. W., Krasting, J. P., Langenhorst, A. R., Zhi, L.,
883 Lin, P., Lin, S. J., Malyshov, S., Mason, E., Milly, P. C. D., Ming, Y., Naik, V., Paulot, F.,
884 Paynter, D., Phillipps, P. J., Radhakrishnan, A., Ramaswamy, V., Robinson, T.,
885 Schwarzkopf, D., Seman, C. J., Shevliakova, E., Shen, Z., Shin, H. H., Silvers, L. G., Wilson,
886 J. R., Winton, M., Wittenberg, A. T., Wyman, B., and Xiang, B.: The GFDL Global

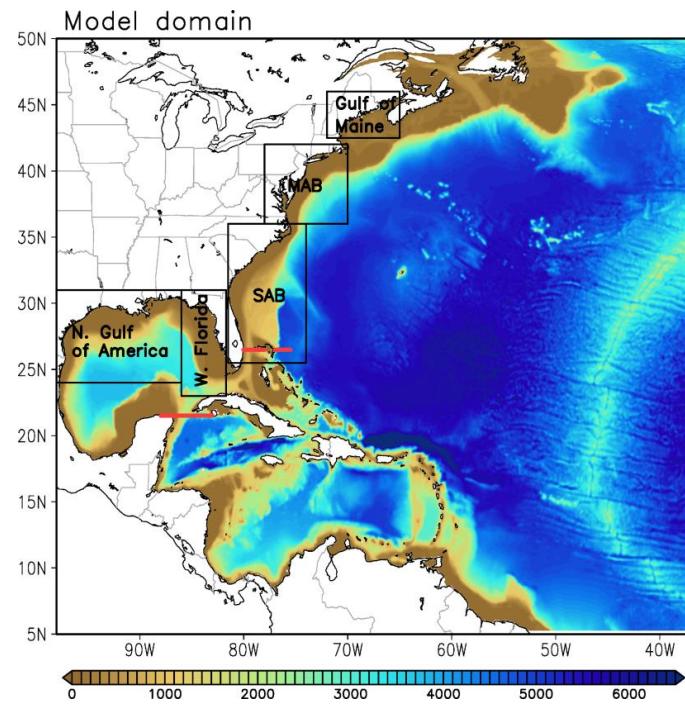


887 Atmosphere and Land Model AM4.0/LM4.0: 1. Simulation characteristics with prescribed
888 SSTs, *Journal of Advances in Modeling Earth Systems*, 10, 691–734,
889 <https://doi.org/10.1002/2017ms001208>, 2018.
890 87. Zhao, M., Golaz, J. C., Held, I. M., Guo, H., Balaji, V., Benson, R., Chen, J. H., Chen, X.,
891 Donner, L. J., Dunne, J. P., Dunne, K., Durachta, J., Fan, S. M., Freidenreich, S. M., Garner,
892 S. T., Ginoux, P., Harris, L. M., Horowitz, L. W., Krasting, J. P., Langenhorst, A. R., Liang,
893 Z., Lin, P., Lin, S. J., Malyshev, S. L., Mason, E., Milly, P. C. D., Ming, Y., Naik, V., Paulot,
894 F., Paynter, D., Phillipps, P., Radhakrishnan, A., Ramaswamy, V., Robinson, T.,
895 Schwarzkopf, D., Seman, C. J., Shevliakova, E., Shen, Z., Shin, H., Silvers, L. G., Wilson, J.
896 R., Winton, M., Wittenberg, A. T., Wyman, B., and Xiang, B.: The GFDL Global
897 Atmosphere and Land Model AM4.0/LM4.0: 2. Model Description, Sensitivity Studies, and
898 Tuning Strategies, *Journal of Advances in Modeling Earth Systems*, 10, 735–769,
899 <https://doi.org/10.1002/2017MS001209>, 2018.
900



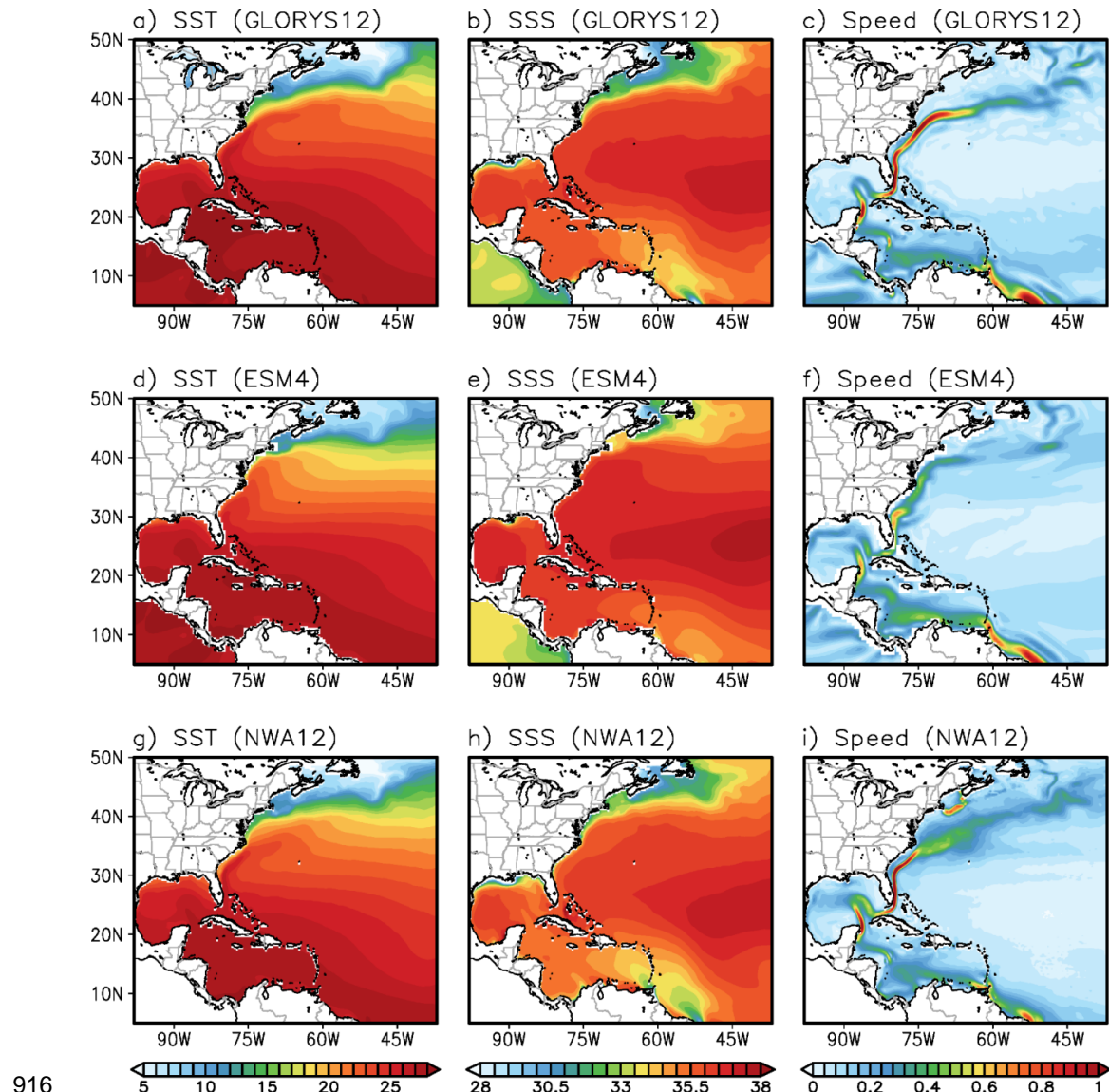
901 Figure list

902

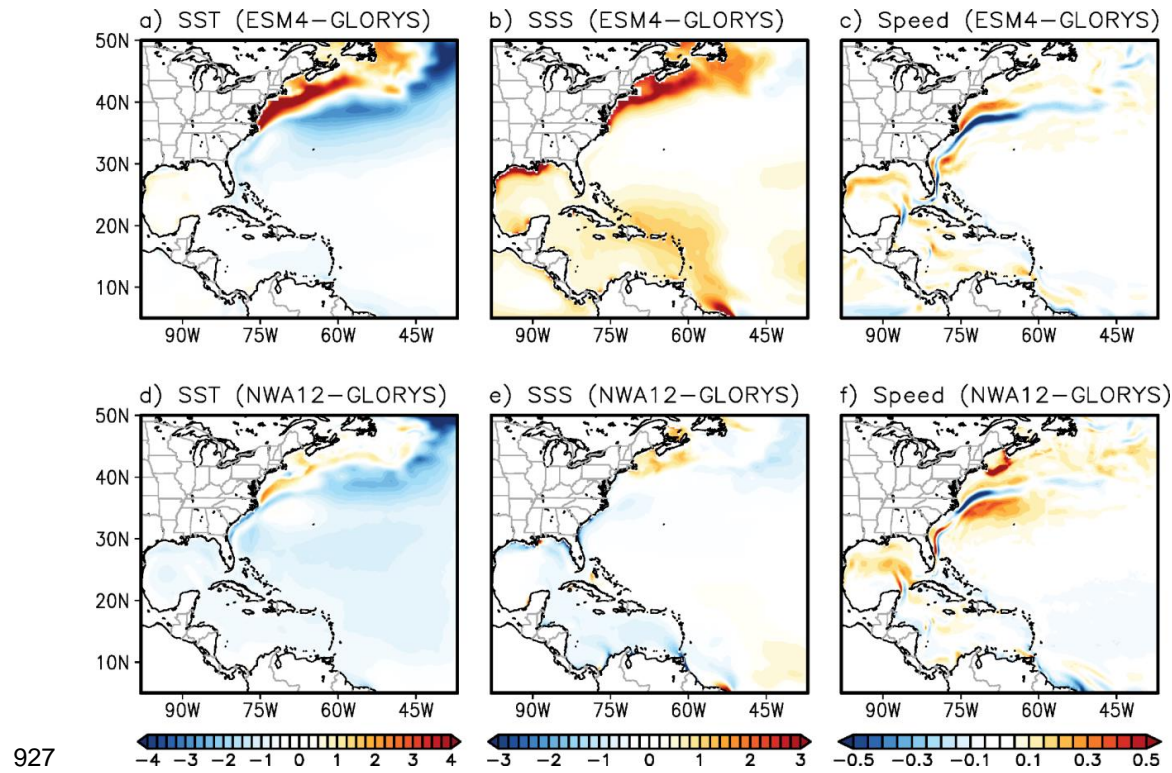


903

904 **Fig. 1.** MOM6-NWA12 model domain and bathymetry (m). The black boxes indicate the
905 location of the Northern Gulf of America, West Florida, South Atlantic Bight (SAB), and middle
906 Atlantic Bight (MAB), and Gulf of Maine for exploring sea-level rise. The red solid lines are the
907 locations of four major Northwestern Atlantic boundary current systems (Yucatan Current,
908 Florida Current, Antilles Current (0~500 m), and Deep Western Boundary Current (1,000-
909 4,000m).
910
911
912
913
914
915



916
917 **Fig. 2.** Spatial pattern of the historical (1993-2020) mean (a) sea surface temperature (SST, °C),
918 Sea surface salinity (SSS, psu), and surface current speed (m s^{-1}) in GLORYS12. (d)-(f) and (g)-
919 (i) are the same as (a)-(c) but in GFDL-ESM4.1, and MOM6-NWA12, respectively.
920
921
922
923
924
925
926



927 **Fig. 3.** Difference of the historical (1993-2020) mean (a) sea surface temperature (SST, °C), (b)
928 sea surface salinity (SSS, psu) and (c) surface current speed (m s^{-1}) between GFDL-ESM4.1 and
929 GLORYS12. (d)-(f) are the same as (a)-(c) but between MOM6-NWA12 and GLORYS12.
930

931

932

933

934

935

936

937

938

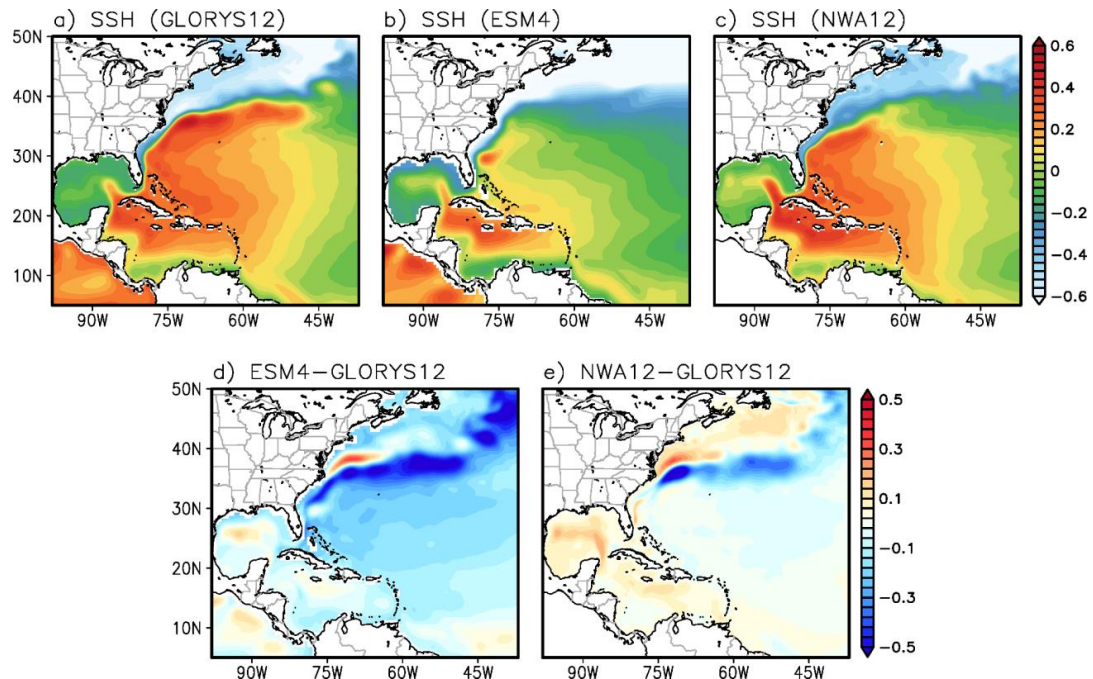
939

940

941

942

943



944

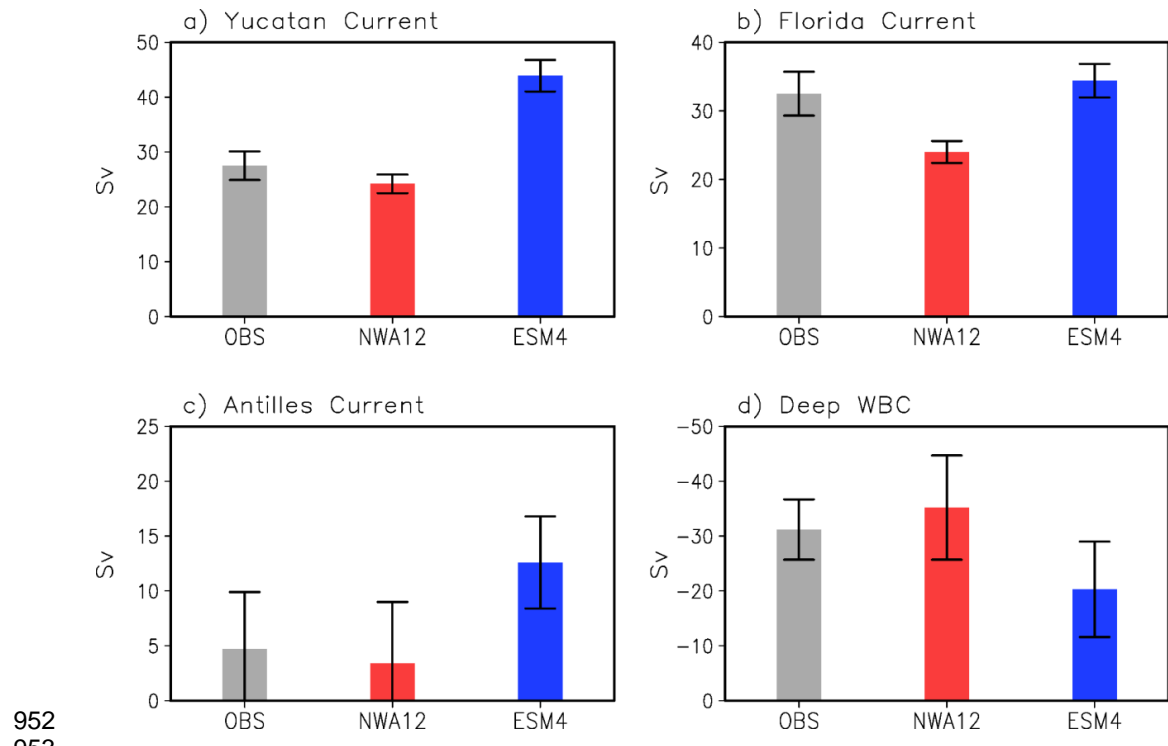
945 **Fig. 4.** Spatial pattern of the historical (1993-2020) mean sea surface height (SSH, m) in (a)
946 GLORYS12, (b) GFDL-ESM4.1 and (c) MOM6-NWA12. (d) The difference between GFDL-
947 ESM4.1 and GLORYS12. (e) difference between MOM6-NWA12 and GLORYS12.

948

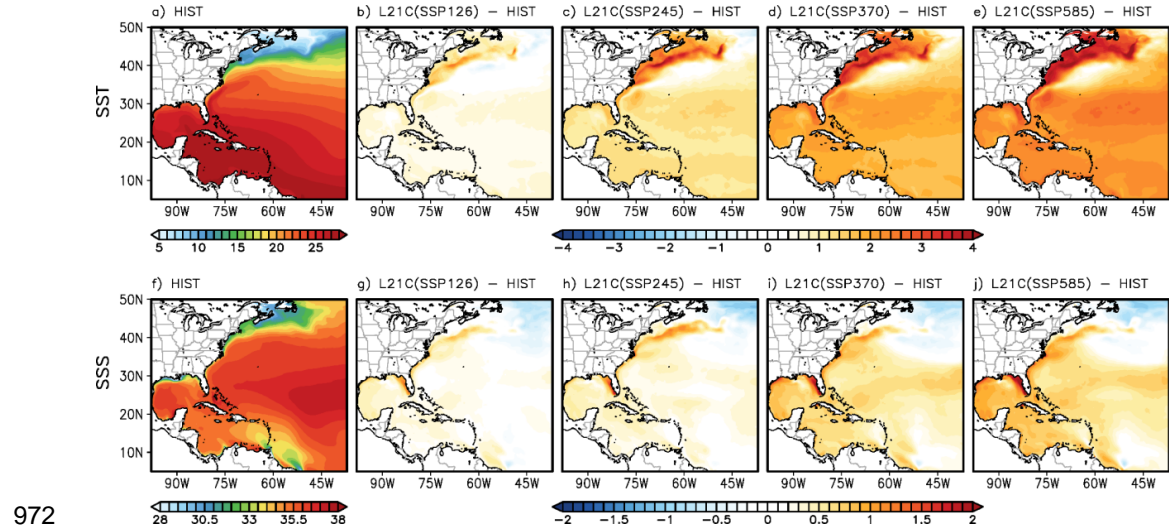
949

950

951



952 **Fig. 5.** The historical mean (1993-2020) of (a) the Florida Current transport, transport across (b)
953 Yucatan Channel, (C) Antilles Current, and (d) Deep Western Boundary Current transport
954 derived from observational records (gray bars), MOM6-NWA12 (red bars) and GFDL-ESM4
955 (blue bars). Note that the observational transport records of the Florida Current, Yucatan Current,
956 Antilles Current, and Deep Western Boundary Current (DWBC) are from Volkov et al. (2024),
957 Athié et al. (2020), Meinen et al. (2019) and Zantopp et al. (2017), respectively.
958
959
960
961
962
963
964
965
966
967
968
969
970
971



972
973 **Fig. 6.** (a) Spatial patterns of sea surface temperature (SST, °C) derived from MOM6-NWA12
974 during (a) historical period (1993-2020). The differences in SST between the future (2073-2100)
975 and historical periods in the (b) SSP-126, (c) SSP-245, (d) SSP-370 and (e) SSP-585 simulations.
976 (f)-(j) are the same (a)-(e) but for sea surface salinity (SSS, psu).

977

978

979

980

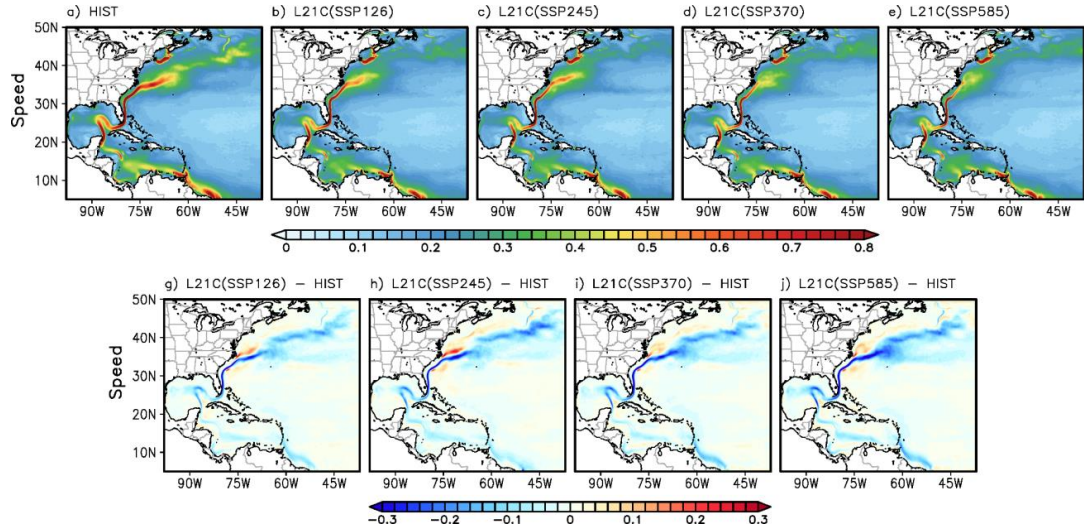
981

982

983

984

985



986

987 **Fig. 7.** Spatial surface current speed (m s^{-1}) patterns derived from MOM6-NWA12 during (a) the
988 historical (1993–2020) period and future (2073–2100) period in (b) SSP-126, (c) SSP-245, (d)
989 SSP-370 and (e) SSP585 simulations. The difference in surface current speed between the future
990 and historical periods in (g) SSP-126, (h) SSP-245, (i) SSP-370 and (j) SSP585 simulations,
991 respectively.

992

993

994

995

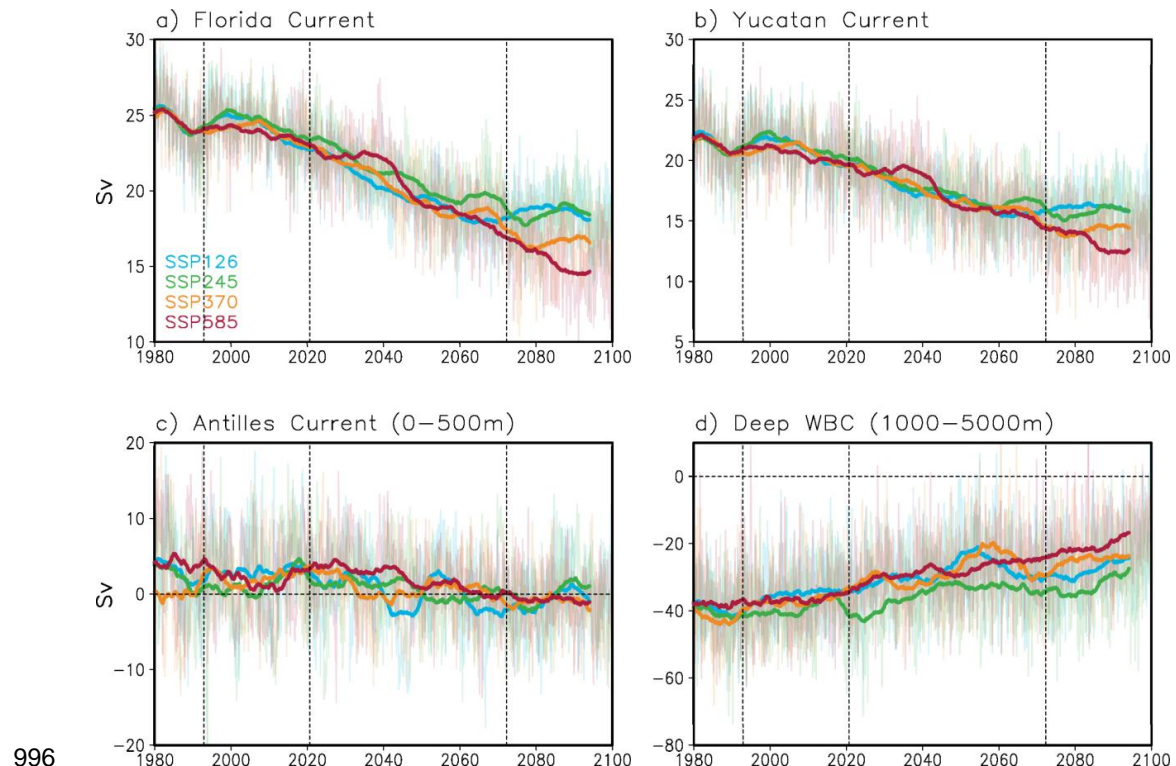
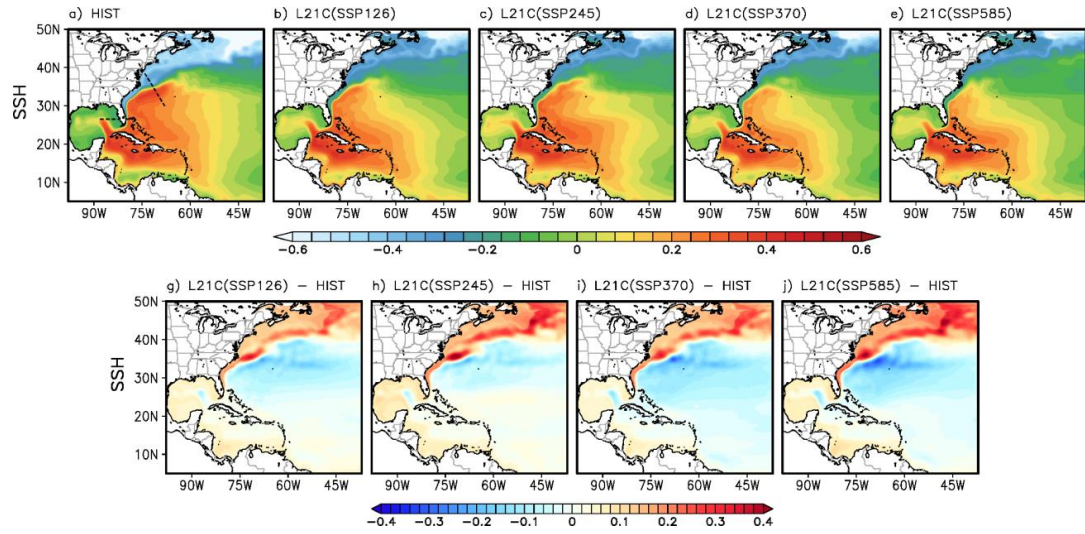


Fig. 8. Time series of (a) the Florida Current transport, (b) transport across the Yucatan Channel, (c) Antilles Current transport and (d) Deep Western Boundary Current transport in MOM6-NWA12. The cyan, green, orange, and red lines are the SSP-126, SSP-245, SSP-370 and SSP-585 simulations, respectively. The bold lines indicate 11-year running means. The dotted lines indicate the historical and future periods. The vertical dotted lines

996
997
998
999
1000
1001
1002
1003
1004
1005
1006



1007

1008 **Fig. 9.** Spatial sea surface height (SSH, m) patterns derived from MOM6-NWA12 during (a) the
1009 historical (1993–2020) period, and future (2073–2100) period from (b) SSP-126, (c) SSP-245, (d)
1010 SSP-370 and (e) SSP-585 simulations. The difference in SSH between the future and historical
1011 periods from (g) SSP-126, (h) SSP-245, (i) SSP-370, and (j) SSP-585 simulations, respectively.
1012 The black dotted lines in (a) indicate the locations of vertical cross-section in Fig.12-14.

1013

1014

1015

1016

1017

1018

1019

1020

1021

1022

1023

1024

1025

1026

1027

1028

1029

1030

1031

1032

1033

1034

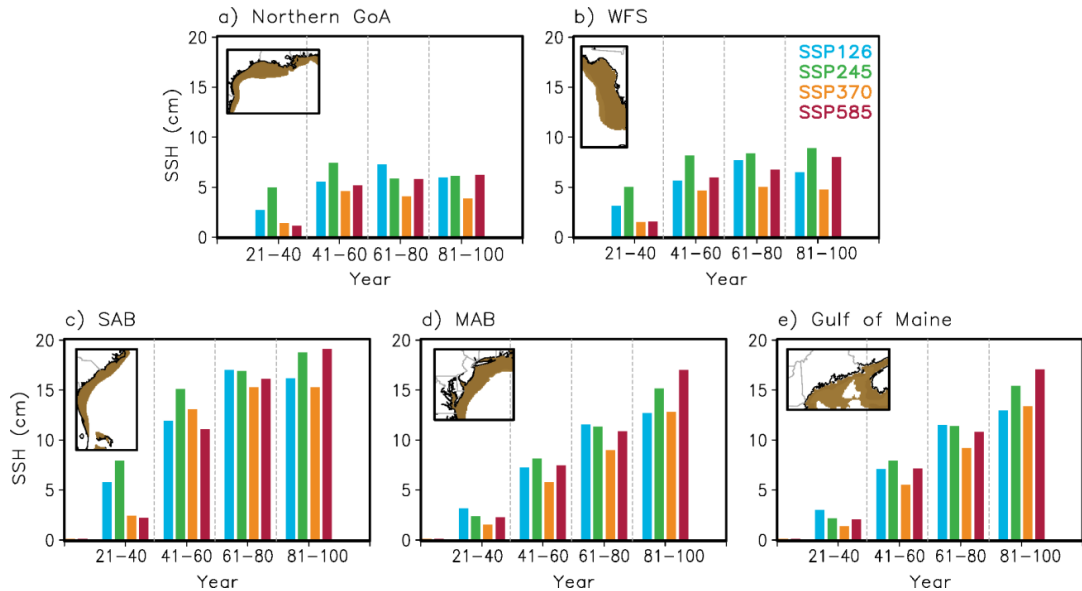


Fig. 10. Spatially averaged sea level changes (cm) in (a) the northern Gulf of America, (b) West Florida shelf, (c) the South Atlantic Bight, (d) the Middle Atlantic Bight, and (e) the Gulf of Maine under the SSP-126 (blue bars), SSP-245 (green bars), SSP-370 (orange bars) and SSP-585 (red bars) simulations. The dynamic sea level changes are spatially averaged over the shelf regions below 200 m depth (brown-colored area in the maps).

1035
1036
1037
1038
1039
1040
1041
1042
1043
1044
1045
1046
1047
1048
1049
1050
1051
1052
1053

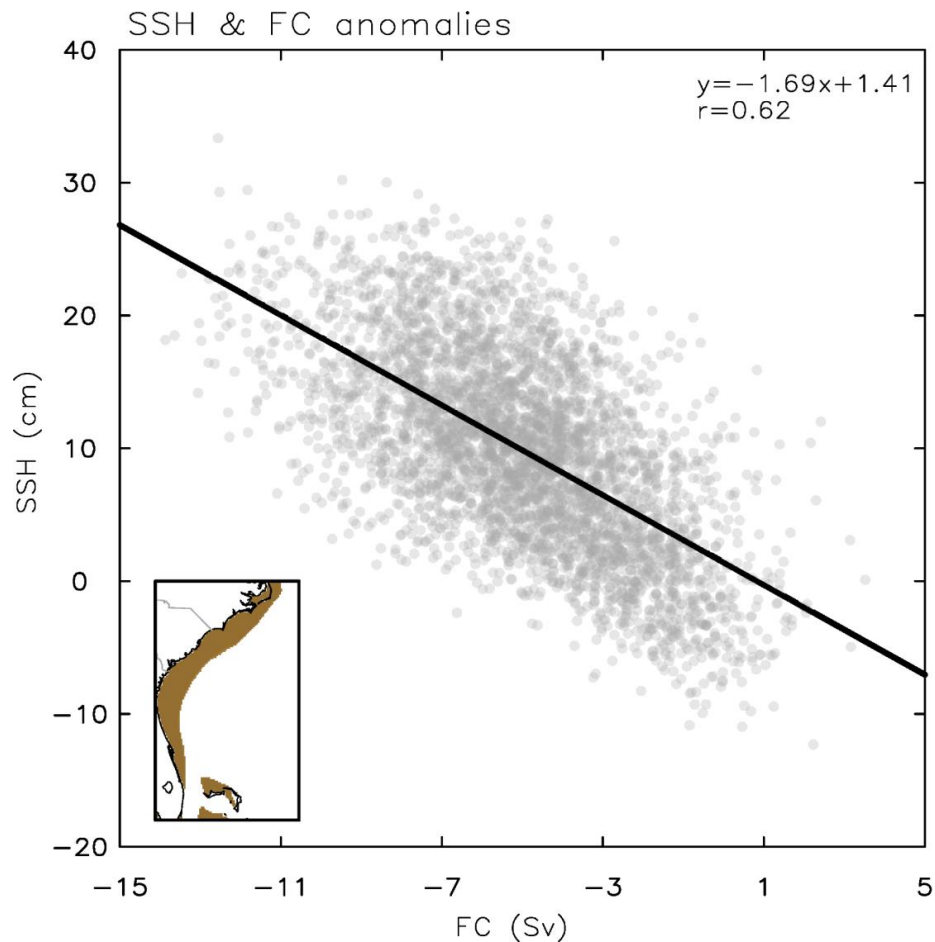
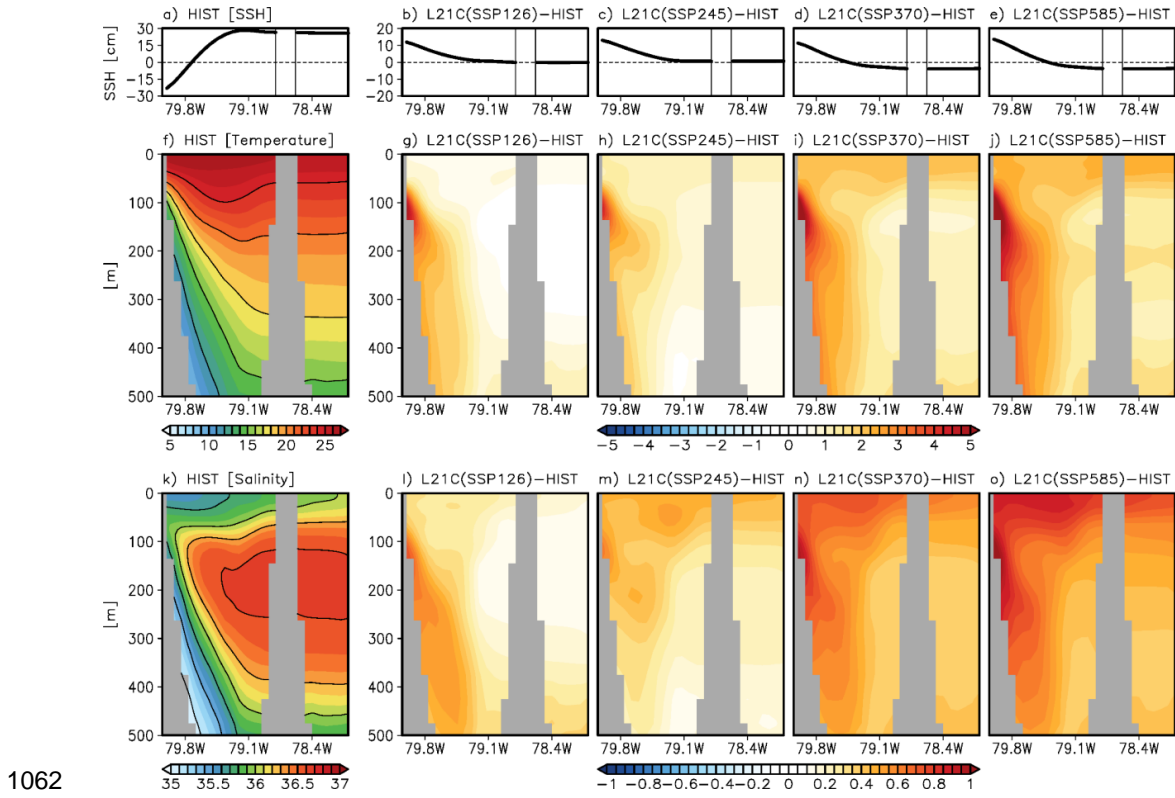


Fig. 11. Scatter plot of anomalous Florida Current (FC) transport (Sv) versus dynamic sea level (cm) change along the South Atlantic Bight derived from all four SSP simulations. The dynamic sea level change is spatially averaged over the shelf regions below 200 m (brown-colored area in the map).



1062

1063

1064

Fig. 12. (a) Sea level at the east coast of Florida (26.5°N , 79.7°W - 78.0°W) during the historical period. Future change in the sea level at the east coast of Florida from (b) SSP-126, (c) SSP-245, (d) SSP-370, (e) SSP-585, and (c) SSP-585 simulations. (f) The vertical cross-sections of the mean temperature across the east coast of Florida during the historical period. The difference in temperature between the future and historical periods from (g) SSP-126, (h) SSP-245, (i) SSP-370, and (j) SSP-585 simulations, respectively. (k)-(o) are the same as (f)-(j) but for salinity.

1070

1071

1072

1073

1074

1075

1076

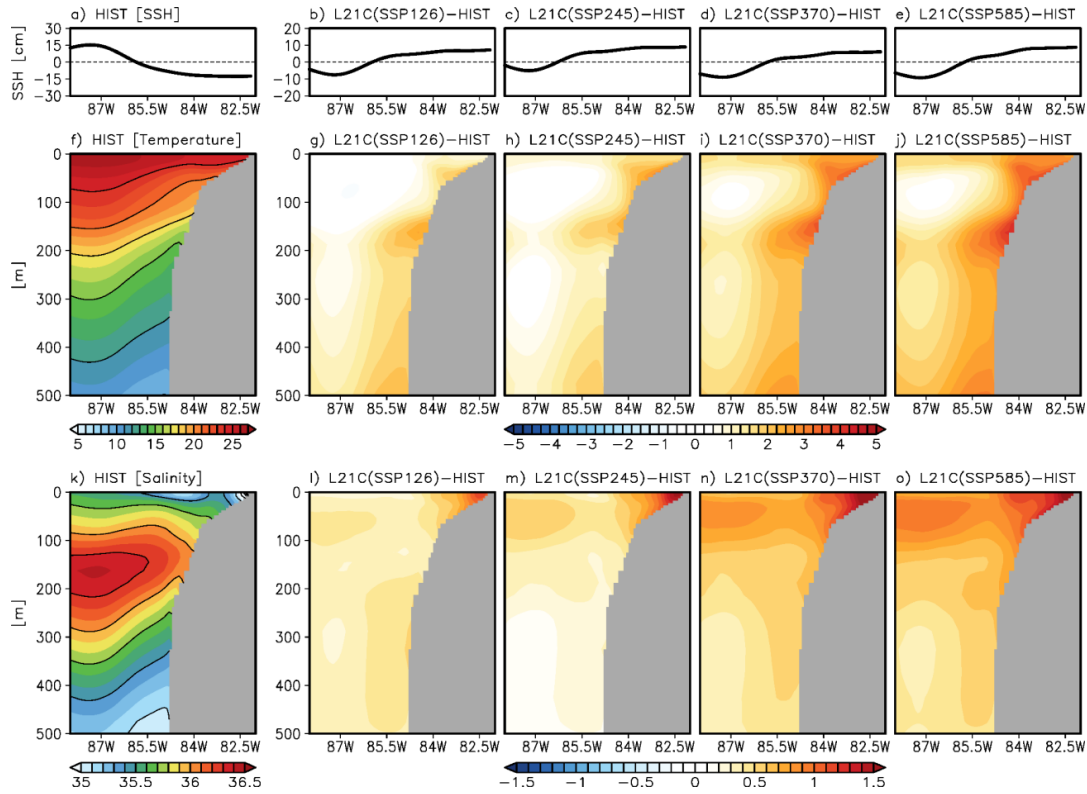
1077

1078

1079

1080

1081



1082

1083 **Fig. 13.** (a) Sea level at West Florida (26.5°N , 88°W - 81°W) during the historical period. Future
1084 change in the sea level at West Florida from (b) SSP-126, (c) SSP-245, (d) SSP-370, (e) SSP-
1085 585, and (c) SSP-585 simulations. (f) The vertical cross-sections of the mean temperature ($^{\circ}\text{C}$)
1086 across West Florida during the historical period. The difference in temperature between the
1087 future and historical periods from (g) SSP-126, (h) SSP-245, (i) SSP-370, and (j) SSP-585
1088 simulations, respectively. (k)-(o) are the same as (f)-(j) but for salinity (psu).
1089

1090

1091

1092

1093

1094

1095

1096

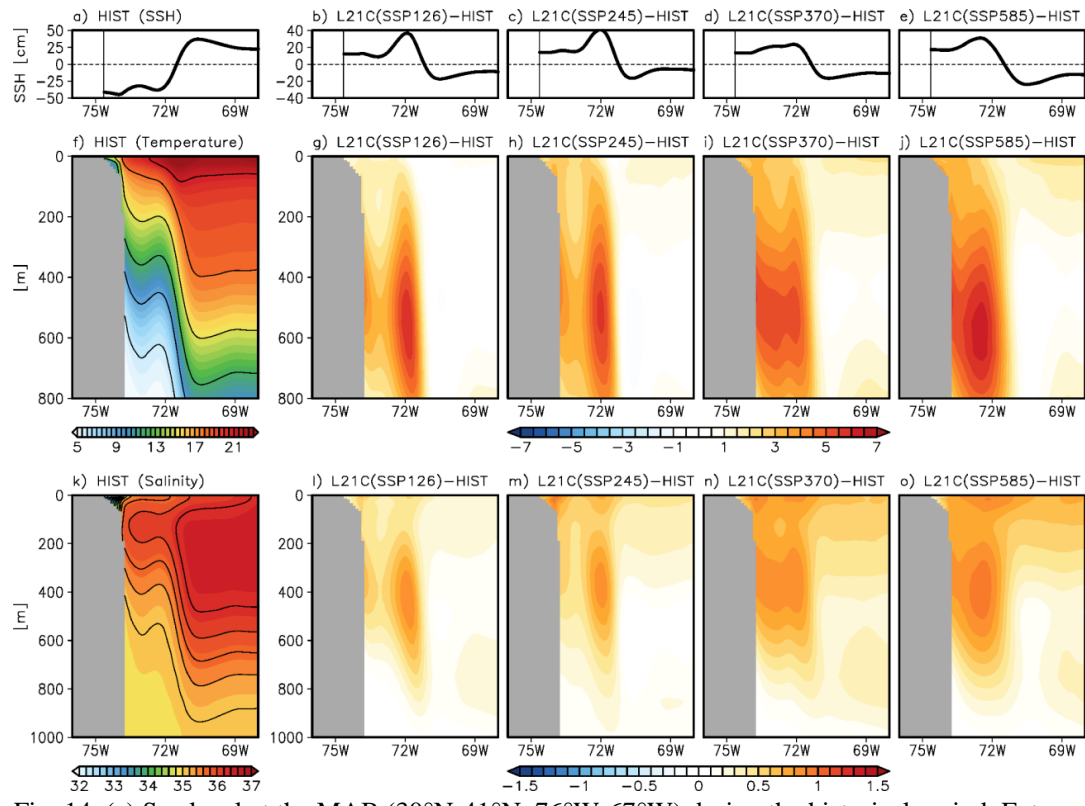
1097

1098

1099

1100

1101



1102

1103 Fig. 14. (a) Sea level at the MAB (30°N-41°N, 76°W-67°W) during the historical period. Future
1104 change in the sea level at the MAB from (b) SSP-126, (c) SSP-245, (d) SSP-370, (e) SSP-585,
1105 and (c) SSP-585 simulations. (f) The vertical cross-sections of the mean temperature (°C) across
1106 the MAB during the historical period. The difference in temperature between the future and
1107 historical periods from (g) SSP-126, (h) SSP-245, (i) SSP-370, and (j) SSP-585 simulations,
1108 respectively. (k)-(o) are the same as (f)-(j) but for salinity (psu).
1109